Optimization of parabolic trough power plant operations in variable irradiance conditions using all sky imagers

B. Nouri[1], K. Noureldin[2], T. Schlichting[3], S. Wilbert[1], T.Hirsch[2], M. Schroedter-Homscheidt[4], P. Kuhn[1],

A. Kazantzidis[5], L.F. Zarzalejo[6], P. Blanc[7], Z. Yasser[8], J. Fernández[9], R. Pitz-Paal[10]

[1]German Aerospace Center (DLR), Institute of Solar Research, Ctra de Senes s/n km 4, 04200 Tabernas, Spain

[2]German Aerospace Center (DLR), Institute of Solar Research, Wankelstrasse 5, 70563 Stuttgart, Germany

[3]German Aerospace Center (DLR), Institute of Solar Research, Solar Power Plant Technology, Prof.-Rehm-Str. 1, 52428 Jülich, Germany

[4]German Aerospace Center (DLR), Institute of Networked Energy Systems, Carl-von-Ossietzky-Straße 15, 26129 Oldenburg, Germany

[5]Laboratory of Atmospheric Physics, Department of Physics, University of Patras, 26500 Patras, Greece

[6]CIEMAT Energy Department – Renewable Energy Division, Av. Complutense 40, 28040 Madrid, Spain

[7]MINES ParisTech, 06904 Sophia Antipolis CEDEX, France

[8]TSK Flagsol Engineering GmbH, Anna-Schneider-Steig 10, 50678 Cologne, Germany

[9]CIEMAT-Plataforma Solar de Almería, Ctra. de Senés km 4.5, E-04200 Tabernas, Almería, Spain

[10]DLR, Institute of Solar Research, Linder Höhe, 51147 Cologne, Germany

Abstract

The continuously growing penetration of intermittent electricity sources will increase the future demand for dispatchable power plants, which balance out fluctuations within the electrical grids. Parabolic trough power plants with thermal energy storages could be one renewable solution for regions with a high yearly direct normal irradiance (DNI) sum, but in order to compete against

other renewable as well as non-renewable technologies, the economic competitiveness must be

ensured. Price reductions can be achieved for example by optimizing the plant operation. One

shortcoming of state of the art plant controllers is that they only use the DNI measured at one or

a few positions in the solar field. Due to the spatial variability of the DNI throughout the solar

field this DNI information can be misleading.

In this paper, we investigate the optimization potential of solar field control strategies with

access to spatially resolved DNI information from all sky imagers (ASI). Uncertainties of the ASI

system are considered by introducing additional independent spatial DNI information from a

shadow camera system. The spatial and temporal DNI variability of the DNI seen by the

controller is classified in distinct DNI variability classes. Two new control strategies are

developed, with optimized control parameters for distinct combinations of the spatial and

temporal DNI variability classes.

We observe significant improvements by these new variability class dependent control

strategies, compared to a state of the art reference controller. A relative increase in revenue in

excess of 1.9% is observed over a test period with 22 individual days.

1 Introduction

The globally installed solar power capacity reached roughly 486 GW (**IRENA 2019**) by the end of 2018. Solar photovoltaic (PV) with about 480 GW is the main contributor compared to 5.4 GW for concentrating solar technologies (**IRENA 2019**). Currently, solar PV is also dominating the overall global capacity increase, with additional 94 GW only in 2018 (**IRENA 2019**). **Kost et al. (2018)** expects a strong continued growth of solar PV reaching a total global capacity between 3000 GW and 9000 GW by the year 2035.

However, the strong growth of intermittent electricity sources, such as solar PV as well as wind power, leads to new technological challenges. Fluctuations may cause unpredictable variations of node voltages and power within the electrical grids, or even instabilities in case of intermediate power shortages (**Woyte et al. 2006; Perez et al. 2016**). Especially small grids are vulnerable to power ramps. Therefore, it comes as no surprise that Hawaii and Puerto Rico already introduced legal limitations for ramp rates (**Gevorgian & Booth 2013; Crăciun et al. 2017**). Larger grids with low penetration of intermittent sources can better compensate fluctuations. But, in a case of a PV penetration above 15% (annual energy basis), significant changes in system operation are required also for large electrical grids (**Denholm & Margolis 2016**).

For regions with high annual direct normal irradiance (DNI) sums, concentrating solar power (CSP) plants with thermal energy storages (TES) provide a dispatchable and renewable energy source (**Platzer 2016**). CSP is therefore capable of balancing fluctuations in electrical grids with high penetration of intermittent sources (**Mehos et al. 2016**).

Yet, whether CSP is going to play an important role in the future global energy mix, is mainly a question of costs. Significant reductions in levelized cost of electricity (LCoE) for CSP with

65 storage were reached in the last couple of years (**Lilliestam & Pitz-Paal 2018**), but the LCoE of

66 solar PV without storage remains significantly lower. However, CSP plants combined with TES

67 outcompete PV plants with battery storage of similar annual production and storage capacity,

68 especially for storage capabilities beyond 6 hours (**Lilliestam et al. 2018**). Such cost

69 comparisons should also take into account that CSP still offers a considerable cost reduction

70 potential. Price reductions can be achieved by scale effects, by improving the component

71 efficiencies or by optimizing the plant operation (**Pitz-Paal 2017**). This study contributes to the

72 latter objective.

73 The operation of commercial CSP power plants offers a lot of opportunities for optimization. In

74 the case of the most common CSP technology, parabolic troughs, collectors concentrate the

75 DNI on receiver tubes. A heat transfer fluid (HTF) circuits the receiver tubes and is heated up to

76 several hundred degrees Celsius. The thermal energy is passed over heat exchangers to a

77 conventional Rankine cycle or TES. Especially intra-hour and intra-minute DNI variability caused

78 by passing clouds pose an operational challenge for commercial parabolic trough power plants

79 with extensive solar field sizes (**García et al. 2011; Hirsch et al. 2014**). An efficient solar field

80 controller needs to find the best combination of field mass flow, temperature set-points and

81 defocusing of collectors corresponding to the prevailing DNI conditions (**Wagner & Wittmann**

82 **2014**). Ideally, a perfect controller would adjust the mass flow in such a way, that the design

83 temperature is always maintained constant without any need of defocusing collectors. In order to

84 approach this ideal, the hydraulic and thermal interactions within the solar field must be well

85 understood - especially under transient conditions with a strong spatial and temporal variability

86 of the DNI inside the solar field.

87　Comprehensive numerical models as developed by **Hirsch & Schenk 2010, García et al. 2011,**

88　**Giostri 2012, Zaversky et al. 2013, Noureldin et al. 2016** and **Noureldin et al. 2017** are useful

89　to study the solar field behavior for distinct control strategies. The so called virtual solar field

90　(VSF), as presented and validated in **Noureldin et al. 2016** and **Noureldin et al. 2017,**

91　simulates the entire solar field in a high temporal and spatial resolution and considers flow

92　maldistribution due to thermal transients and DNI inhomogeneity as reported e.g. in **Abutayeh**

93　**et al. 2014.** Furthermore, the VSF is designed to consider spatially inhomogeneous DNI

94　information, which occur during transient conditions and have a significant impact on the solar

95　field behavior.

96　Such spatially resolved DNI information can be provided by camera based monitoring and

97　nowcasting systems. These systems provide an intra-minute temporal resolution and a spatial

98　resolution ≤ 20 m. The most common nowcasting systems consist of upward-facing all sky

99　imagers (ASI) (**Chow et al. 2011; Quesada-Ruiz et al. 2014; Peng et al. 2015; Blanc et al.**

100　**2017**; **Kazantzidis et al. 2017; Nouri et al. 2019b**). The principle method of these ASI systems

101　is most often similar. Images of the complete sky are taken and clouds are detected. If the

102　system consists of more than one ASI, the cloud height is determined via stereo photography or

103　similar approaches. Cloud shadows are projected to a ground model. The resulting shadow

104　maps are converted into irradiance maps via local irradiance measurements. For irradiance

105　predictions clouds can be tracked over consecutive sky images.

106　A less common and distinct nowcasting approach uses downward-facing cameras (**Kuhn et al.**

107　**2017b**). These so called shadow cameras are mounted on an elevated position and take images

108　of the ground. Shadow maps are created by detecting the cloud shadows within the ground

109　images. The shadow maps are converted into irradiance maps via local irradiance
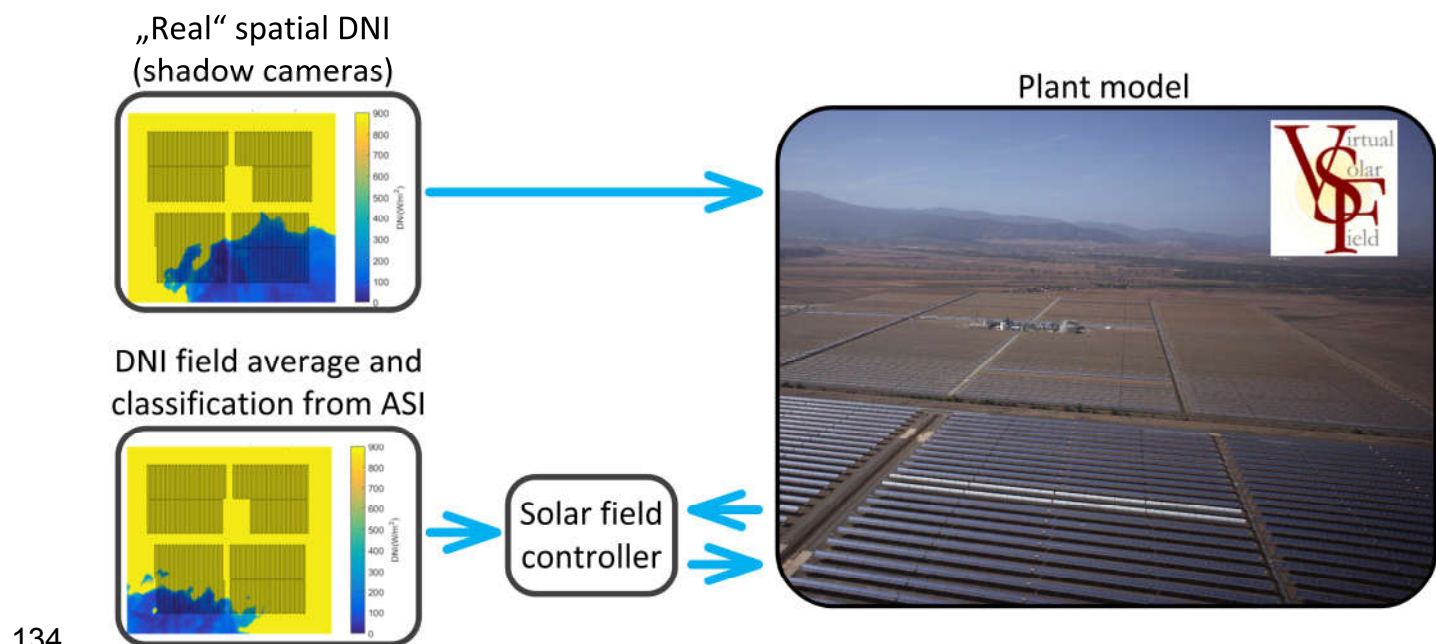
110   measurements and fully shaded as well as fully clear reference images taken for the same solar

111   position.

112   **Noureldin et al. 2019a** investigated the possible benefit of a parabolic trough solar field

113   controller with access to perfectly accurate spatial DNI information compared to a state of the art

114   controller with DNI information only from one or handful reference pyrheliometers distributed in

115   the solar field. **Noureldin et al. 2019a** utilizes the VSF and DNI maps from the ASI system

116   described by **Nouri et al. 2019b.** This initial study showed a significant potential with an

117   estimated gain in revenue up to 2.5% for some days with variable conditions. However, the

118   results presented in **Noureldin et al. 2019a** treat the DNI maps from the ASI system as perfectly

119   accurate descriptions of the ambient conditions. Yet, uncertainties exist, which also depend

120   strongly on the prevailing weather conditions (**Marquez & Coimbra 2013**).

121   In this study, we will investigate the actual benefit of spatial DNI information from ASI systems

122   for a parabolic trough solar field controller with consideration of the system uncertainties. The

123   ASI derived DNI maps are provided to the solar field controller as DNI field average and a DNI

124   variability classification. The solar field controller is then adjusted according to the prevailing

125   spatial and temporal DNI variability class.

126   The uncertainties of the ASI system are considered by including additional spatial DNI

127   information from the fundamentally distinct shadow camera system (**Kuhn et al. 2017b**), which

128   provides the actual DNI conditions acting on the solar field, whereas the solar field controller will

129   receive only the DNI information from the ASI system (see Figure 1). Ideally, this allows the

130   quantification of the achievable impact of ASI based control schemes, with actual divergent

131   weather conditions unknown by the solar field controller. Of course, the shadow camera system

132 is not perfect by itself but validation results illustrate that it outperforms the ASI systems and can

133 therefore be used as reference (see section 2.2).

"Real" spatial DNI
(shadow cameras)

Plant model

DNI field average and
classification from ASI

Solar field
controller

134

137 The ASI system also provides predictions up to 15 minutes ahead, which could be utilized by

138 model predictive controllers. Nevertheless, in this work we investigate only the potential benefit

139 of solar field control schemes with access to spatial DNI information of the current conditions.

140 All the presented evaluation strategies, including the ASI system and the VSF simulations, are

141 quasi real time capable with an average overall processing time of roughly 7 seconds per time

142 stamp (8x3.6GHz Intel Core i9-9900K, 2x16GB DDR4-2666 and PNY Quadro RTX 4000 8GB

143 GDDR6). The fast processing time allows the solar field controller to obtain updates of the

144 irradiance situation in a timely manner.

145 Section 2 and section 3 of this paper will give an overview on the used ASI system and the VSF,

146 respectively. The developed temporal and spatial DNI variability classification method is

147 presented in section 4. Two new solar field control strategies based on the DNI variability

148 classes are presented and evaluated versus a reference controller in section 5. These new

149 controllers are tailored to a solar field design according to the Spanish commercial 50 MW

150 power plant La Africana. In section 6, we identify applicability conditions of the new variability

151 class dependent control strategies and present the performance results of a hybridized control

152 strategy. Finally section 7 concludes the paper.

153 ## 2 Overview on used camera systems that provide DNI maps

154 Two different sources for spatially and temporally resolved DNI information are used in this

155 study. Whereas the information of the ASI system is used as the available DNI information,

156 provides the shadow camera system the "real" DNI over the solar field. The following sections

157 introduce these two irradiance measuring devices.

158 ### 2.1 All sky imager system

159 The used ASI system consists of two Mobotix Q24 of-the-shelf surveillance cameras and the

160 DNI information of a Kipp&Zonen CHP1 pyrheliometer. The cameras are operated at CIEMAT's

161 Plataforma Solar de Almería (PSA) and mounted 494 m apart from each other. One of the

162 cameras stands at a distance less than 8 m away from the pyrheliometer. Q24 cameras are

163 equipped with fisheye lenses for taking hemispheric images of the sky. All sky images with a 3-

164 mega pixel resolution (see Figure 2) are taken simultaneously by both cameras every 30
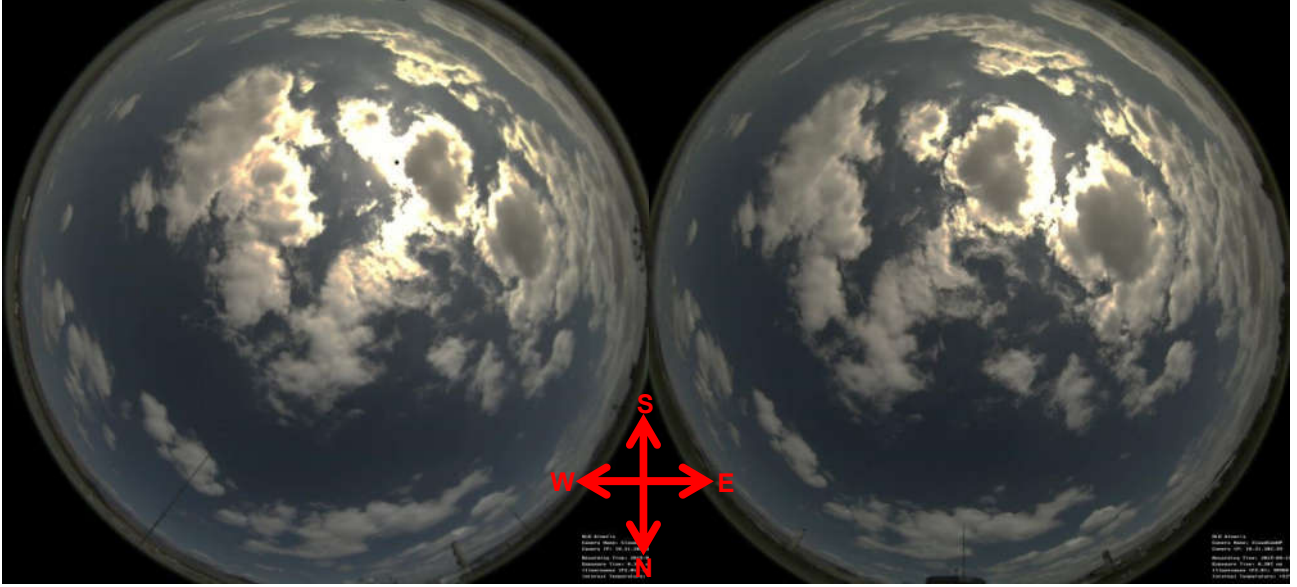
165 seconds.

Figure 2: Example sky images as taken simultaneously by both Mobotix Q24 cameras

The image processing treats each detected cloud as an individual object with the attributes position, motion, and transmittance as described in **Nouri et al. 2018b**. Clouds in the sky are segmented by means of a four dimensional clear sky library (**Wilbert et al. 2016**; **Kuhn et al. 2017a**) which accounts for different atmospheric conditions. Geolocation and motion of the clouds is detected by a stereoscopic approach based on differential images (**Nouri et al. 2019a**). A binary shadow map is created via a raytracing algorithm (**Nouri et al. 2018b**). A probabilistic approach utilizes current and historical cloud transmittance and cloud height measurements to allocate actual cloud transmittance values (**Nouri et al. 2019b**). Finally, a binary shadow map is converted into a DNI map by introducing the current clear sky DNI and the corresponding cloud transmittance values.

In the current configuration the DNI maps have an edge length up to 8 km with a spatial resolution down to 5 m. The overall ASI system and its sub systems were validated intensively. Overall relative mean absolute deviation (MAD) of 4% and root mean square deviation (RMSD)

9

181   of 7.8% are reached for the current conditions (lead time 0 minutes) over a two year period,

182   compared with three spatially distributed reference pyrheliometers (**Nouri et al. 2019b**).

183   2.2   Shadow camera system

184   ASI systems need to detect the position of clouds in the sky accurately in all three spatial

185   dimensions. Complex but common and frequently changing atmospheric conditions, partially

186   with multiple cloud layers, make this task challenging. A unique alternative to ASI systems are

187   shadow camera systems, which detect directly the cloud shadows on the ground, without the

188   detour over the clouds in the sky. The method and its validation is described in **Kuhn et al.**

189   **2017b**, possible applications are presented in **Kuhn et al. 2019**. At the Plataforma Solar de

190   Almeria (PSA) in Spain both the ASI system as described in section 2.1 and the shadow camera

191   system are operated jointly. The shadow camera system consists of six Mobotix M24 off-the-

192   shelf surveillance cameras mounted on the top of a 87 m high solar tower. Figure 3 shows one

193   of the shadow cameras and an example image as taken from the tower looking to the ground.

194

195   **Figure 3: (left) Shadow camera mounted on top of a solar tower (right) image of a shadow camera**

196   The viewing cones of the six cameras cover a 360° view around the tower. All cameras take

197   simultaneously every 15 seconds a new image of the ground which are converted to a single

198   orthoimage (Figure 4).

199

Figure 4: Orthoimage with a 360° view created from images of six shadow cameras mounted on the top of a solar tower.

201 A difference image is calculated between the actual orthoimage and an additional reference

202 clear sky orthoimage from a data base corresponding to a similar Sun position with less than 3°

203 deviation of azimuth and elevation angle. Furthermore, the reference image must be taken less

204 than 60 days before the current image, which avoids significant differences in ground properties.

205 Shadows on the ground are segmented by comparing each pixel value of the difference image

206 with empirically identified thresholds. The shadow camera system uses the DNI measurements

207 taken by a pyrheliometer and DHI measurements taken by a pyranometer with a shadow ball.

208 Unshaded sections of the orthoimage receive the clear sky DNI values identified by the most

209 recent clear DNI measurements detected according to **Hanrieder et al. 2016.** For the

210 identification of the DNI within the shaded sections a second reference orthoimage image for

211 overcast conditions is needed. The second reference image must be taken in the last 60 days

212 and within 10° of the Sun elevation and azimuth angle for the evaluated image. The DNI in the

213 shaded pixels is calculated according to **Kuhn et al. 2017b** from the rgb values of the three

214 orthoimages and the DHI measurement. The sunny and the shaded reference image are used to

215 approximate the bidirectional reflectance distribution function of each pixel in the image for the

216 current solar position and the position of the camera. The final DNI maps have a spatial

217 resolution of 5 m with a maximum edge length of 2 km.

218 A benchmarking campaign between the ASI system described in section 2.1 and the shadow

219 camera system with three reference pyrheliometer over 22 variable days was conducted by

220 **Kuhn et al. 2019**. For lead time 0 minutes, the shadow camera system reached a rel. RMSD of

221 10.2%, rel. MAD of 6.7% and a rel. bias of 3.3% compared to a rel. RMSD of 15.1%, rel. MAD of

222 9.2% and a rel. bias of 6.7% for the ASI system.

3 Virtual Solar Field

3.1 Overview of virtual solar field

225 Parabolic trough solar fields of commercial power plants are spatially extended facilities with

226 edge lengths typically above 1 km. The solar field is divided into several sections, whereas each

227 section consists of a multitude of parallel loops. Each loop itself consists of several solar

228 collector assemblies (SCA), which describe the smallest collector unit with an independent drive

229 for tracking. The incoming DNI is concentrated by parabolic shaped collectors to the focal line.

230 Receiver tubes are located in the focal line. A heat transfer fluid circulates through the receiver

231 tubes. All loops of the same section are connected to a cold and a hot section header pipe. In

232 turn, all the section header pipes are connected to a cold or hot main header pipe, which

233 connects the solar field sections to the power block. A schematic solar field layout is illustrated in

234 Figure 5. The control of such a solar field is a complex hydraulic as well as a thermal challenge.

235 The loops of the solar field are not equipped with individual flow control valves. This means that

236 the flow through the field is only determined by the power of the main pump supplying the whole

237 solar field. The flow distribution over the sectors and loops is thus defined by the hydraulic

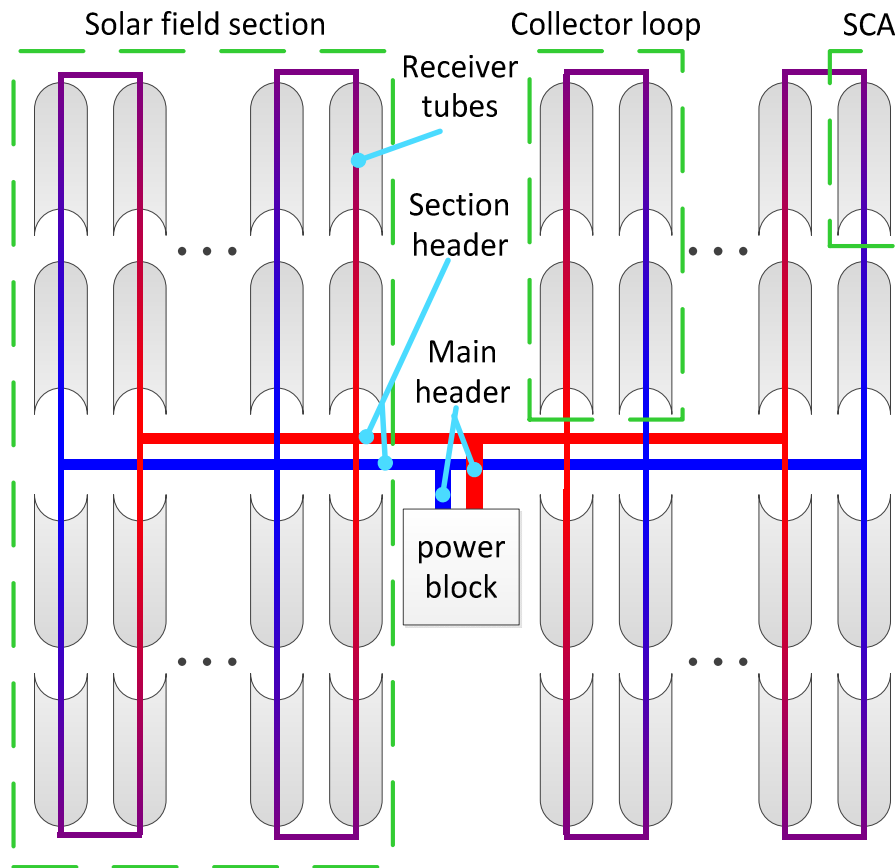238 resistance of each of the parallel loops in the network.

Figure 5: Schematic solar field layout

The VSF is a simulation environment which models the entire solar field from the power block. Common solar field designs with an arbitrary number of loops can be realized with the VSF software. In order to accurately predict the physical behavior of the solar field, VSF couples a hydraulic network solver with a thermal solver. A detailed description of VSF can be found in **Noureldin et al. 2016** and **Noureldin et al. 2017.** The VSF principles and the existing validation of the VSF are summarized below.

The hydraulic solver computes the flow distribution within the branched piping system based on steady state assumptions. For this purpose, the solar field is discretized in pipe elements of 12.5 m length within the collectors and 15 m to 50 m length within the header piping. Due to strong variations in temperature within the solar field (also during stable conditions), the

251   hydraulic resistance is computed for each discrete element with a temporal resolution of 2

252   seconds. Therefore, VSF is also capable of characterizing flow maldistribution due to thermal

253   transients as e.g. triggered by variable solar irradiance conditions or fluid distributions due to

254   inhomogeneities in plant design or operations.

255   The hydraulic solver passes flow boundary conditions to the thermal solver, which in turn

256   dynamically computes the temperatures with respect to the local thermal and operation

257   conditions, and the thermal losses within each discrete pipe element. These calculations solve

258   the time-dependent continuity and energy equations based on the assumption of a one

259   dimensional flow. Previously published empirical relations are utilized for the thermal losses (e.g.

260   **Burkholder and Kutscher 2009** for Schott PTR-70 receiver tubes). At pipe intersections the

261   temperatures are computed by enthalpy balancing.
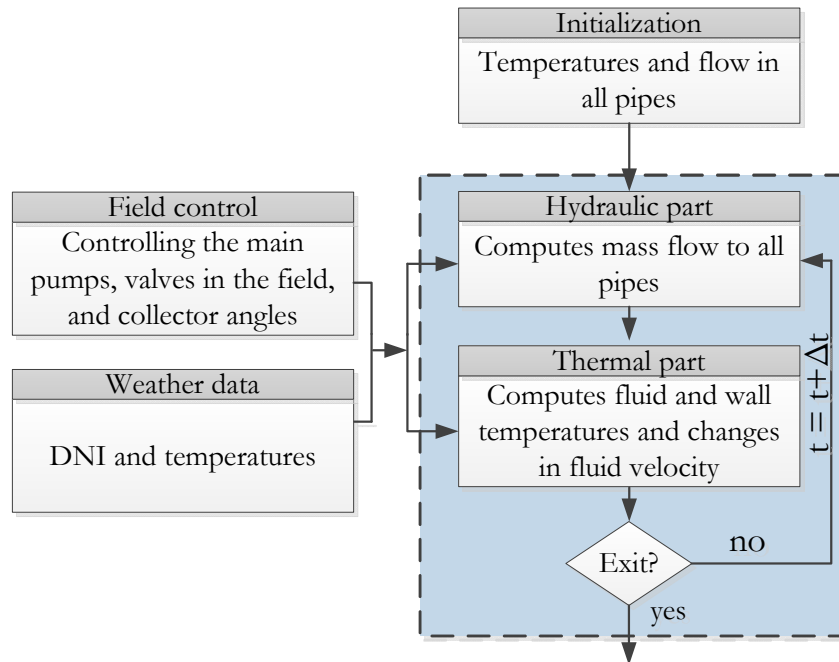

262

263   **Figure 6: Illustration of the VSF program flow (adapted from Noureldin et al. 2018a)**

264   A comprehensive validation of VSF was conducted based on a few days in Spring 2015 and real

265   plant operations data from the 50 MW parabolic trough power plant Andasol-3 located in

14

266 southern Spain (**Noureldin et al. 2017)**. This power plant consists of four subfields with 38 loops

267 each. The power plant data were supported by additionally measured values from a

268 measurement campaign carried out simultaneously by the DLR at Andasol 3 on three test loops

269 (**Noureldin et al. 2016**). These additional data provide flow and temperature measurements

270 within the test loops with a high temporal resolution. For this purpose the loops were equipped

271 with a FLEXIM FLUXUS ADM 6725 clamp on ultrasonic flow meters with wave injectors for high

272 temperature applications at the loop center (cross over piping) and a clamp-on temperature

273 measuring system based on PT100s at the loop inlet and outlet (**Nouri et al. 2018a**). The

274 validation was conducted over distinct cases including normal operations with predominantly

275 clear conditions, start-up situations in clear mornings and conditions with strong transients due

276 to cloud passages. For the flow distribution, deviations below 5% between the simulated and

277 measured values were observed. During normal operations an overall RMSD in fluid

278 temperature of 2.75 K is observed. The RMSD rises up to 9.7 K during strong defocusing cycles.

279 These deviations are not significant compared to the expected uncertainties of the power plant

280 instrumentation (**Janotte 2012**).

281 ## 3.2   Solar field controller assessment with the VSF

282 VSF is a useful tool to comparatively assess distinct solar field controllers in terms of the yield.

283 In **Noureldin et al. 2018b** and **Noureldin et al. 2019a** an approach is presented, which allows a

284 monetary assessment of parabolic trough solar field controller with the results of VSF

285 simulations. The solar field control concept is described in section 5. We will roughly summarize

286 the evaluation approach here, for the better understanding of the results presented in sections 5

287 and 6. Since the mass flow can only be altered for the whole field but not for each individual

288 loop, inhomogeneous irradiance conditions or flow distribution may cause some loops to

289 temporarily overheat while others do not reach the set point temperature. A methodology based

290   on economic penalties has been developed to assess the solar field controller quality. The total

291   economic penalty is composed as

$$p_{tot} = p_{def} + p_{T,PB} + p_{TES}..$$

<div align="right">**Equation 1**</div>

292   The first term p_{def} describes a loss of revenue due to defocused collectors where the amount of

293   not usable heat Q_{def} is weighted with the power block $\eta_{PB,a}$ efficiency and levelized cost of

294   electricity $LCoE$,

$$p_{def} = Q_{def} \cdot \eta_{PB,a} \cdot LCoE \ .$$

<div align="right">**Equation 2**</div>

295   The second effect is given by the fact that any reduction in solar field outlet temperature leads to

296   a reduction of the power block efficiency. The overall heat produced by the solar field is again

297   weighted with the LCoE and the averaged power block efficiency corrected by temperature

298   effects. The reduced power block efficiency penalty $p_{T,PB}$ is described by

$$p_{T,PB} = Q_{th,SF} \cdot \eta_{PB,a} \cdot LCoE \cdot \left(1 - \frac{\eta_{PB,T}}{\eta_{PB,T_0}}\right)$$

<div align="right">**Equation 3**</div>

299   with $Q_{th,SF}$ as the thermal solar field energy, η_{PB,T_0} the power block efficiency at the design

300   temperature and $\eta_{PB,T}$ as the power block efficiency at the current temperature.

301   Reduced solar field temperatures have also an effect on TES efficiency. This is due to an overall

302   lower average temperature within the hot tank of the TES. This effect can be described by the

303   TES penalty

$$p_{TES} = Q_{th,SF} \cdot \eta_{PB,a} \cdot LCoE \cdot \left(1 - \frac{T_{out} - T_{in}}{T_0 - T_{in}}\right) \cdot \frac{Q_{OL,a}}{Q_{TES,a}}$$

<div align="right">**Equation 4**</div>

304　with T_{out} as the solar field outlet temperature, T_{in} as the solar field inlet temperature, T_0 as the

305　design temperature for the solar field outlet and $\frac{Q_{OL,a}}{Q_{TES,a}}$ as the annually averaged ratio of TES

306　overload resulting in solar energy dumping.

307　The quantities $\eta_{PB,a}$, $LCoE$ and $\frac{Q_{OL,a}}{Q_{TES,a}}$ are determined as average values over one year by means

308　of annual yield simulations conducted with the Greenius simulation software (**Dersch et al.**

309　**2012; Dieckmann 2017**). For the La Africana power plant considered in sections 5 and 6, the

310　following values are used $\eta_{PB,a} = 0.25$, $LCoE = 192.5 \frac{€}{MWh}$ and $\frac{Q_{OL,a}}{Q_{TES,a}} = 0.33$. The theoretical

311　revenue R_{th} and the actual revenue R_{SF} are calculated according to the Equation 5 and Equation

312　6.

$$R_{th} = \eta_{PB,a} \cdot LCoE \cdot \sum_{SCA} \int \left[G_{eff}(t) \cdot \eta_{opt} \cdot A_{ap} \right]_{SCA} dt \qquad \textbf{Equation 5}$$

$$R_{SF} = \eta_{PB,a} \cdot LCoE \cdot \int \dot{Q}_{th,SF} dt - \left(p_{TES} + p_{T,PB} \right) \qquad \textbf{Equation 6}$$

313　Thermal losses in the field are computed as

$$Q_{loss,oth} = R_{th} - p_{def} - \eta_{PB,a} \cdot LCoE \cdot \int \dot{Q}_{th,SF} dt \qquad \textbf{Equation 7}$$

314　with G_{eff} as the effective solar irradiance falling on the collector, η_{opt} as the optical collector

315　efficiency and A_{ap} as the collector aperture area.

4 DNI variability classes

4.1 Temporal variability classes

Temporal DNI variability classes are introduced to categorize irradiance situations based on the prevailing variability in the solar resource. They can be used for systematic analysis and, as in this study, for selecting situation dependent controllers.

The temporal DNI variability classification is determined according to the procedure described in **Schroedter-Homscheidt et al. 2018** with the adaptations described in **Nouri et al. 2019c**. This approach analyses 13 distinct variability indices and classifies the DNI in one of eight classes form clear sky (class 1) to overcast (class 8). The definition of the distinct classes is given in Table 1. Each time stamp is classified by analyzing the DNI information of the previous 15 minutes (1 minute average DNI values).

Table 1: Description temporal DNI variability classes

Class	Variability	Clear sky index (DNI/DNI_{clear})	General description
1	Low	Very high	Clear sky
2	Low	High	Almost clear sky
3	Intermediate	High/Intermediate	Almost clear sky
4	High	Intermediate	Partly cloudy
5	Intermediate	Intermediate	Partly cloudy
6	High	Intermediate/Low	Partly cloudy
7	Intermediate	Low	Almost overcast
8	Low	Very Low	Overcast

As an example we show in Figure 7 the DNI, clear sky DNI and the corresponding temporal DNI variability class for the 09.09.2015 (PSA). The forenoon of this day is mainly dominated by clear

331 sky conditions. More variable conditions start shortly before 11 UTC. The afternoon shows high

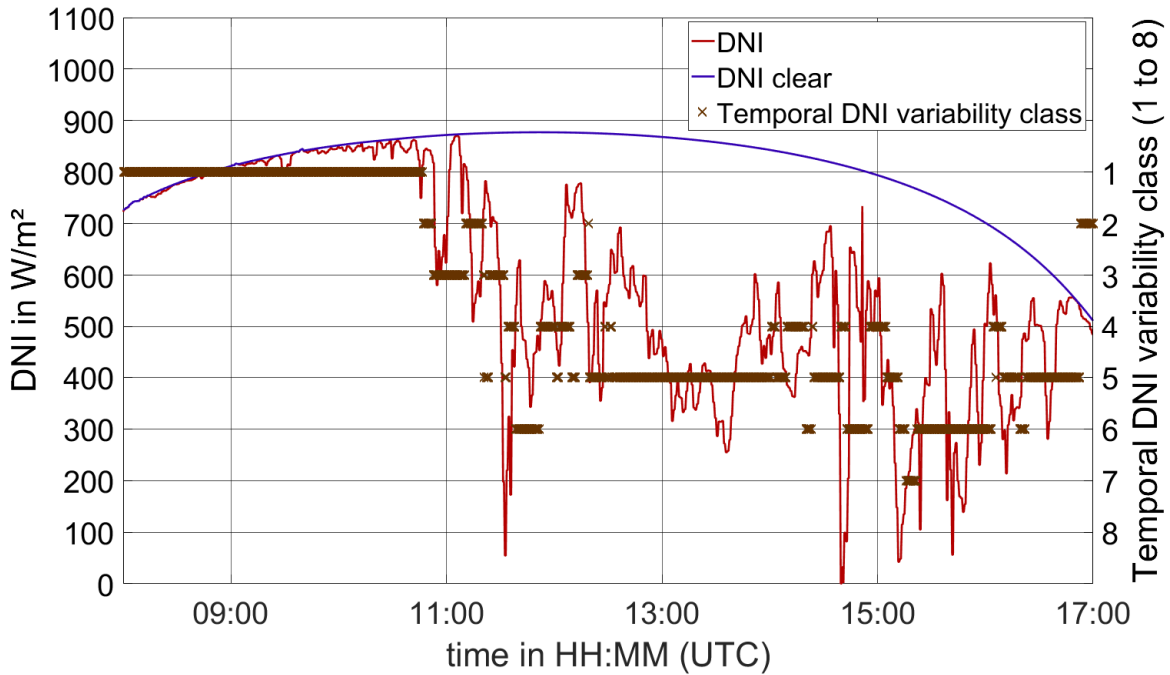332 and intermediate variability conditions mainly dominated by class 5.

Figure 7: Temporal DNI variability classes of an example day (09.09.2015)

4.2 Spatial variability classes

336 The temporal variability classification is a method to describe the temporal variability as

337 observed in a ground observation, but it does not describe the spatial pattern involved in detail.

338 The impact of spatial heterogeneity of DNI on the solar field can be severe even if the temporal

339 variability is low. For example, conditions could occur where only half of the solar field is shaded

340 by clouds with a low transmittance while the other half is fully illuminated. From the viewpoint of

341 temporal variability, the situation is not variable at all if the cloud is not moving horizontally, or it

342 presents a low temporal variability if the cloud edge moves across the ground observation

343 pinpoint.

19

344   In such a case, the two pyrheliometers used for a control may be placed one in the shaded and

345   one in the sunny area. The controller will adjust the flow of the HTF according to the average

346   solar field DNI. This leads to a partial cooling and overheating of the solar field which in turn

347   leads to a flow maldistribution. An even stronger imbalance between shaded and sunny shares

348   of the solar field could increase this issue – if not known to the controller. Especially problematic

349   are profound overheating issues within sunny parts of the solar field, causing defocusing and

350   energy dumping. The share between shaded and unshaded parts of the solar field is therefore a

351   decisive value for the solar field behavior and requires a specific treatment. Therefore, two new

352   variability indices derived from spatial DNI maps are introduced.

353   •   The shadow area fraction S_A describes the relative shaded share of the solar field

354   ○ $S_A = \frac{A_{SASF}}{A_{SF}} \cdot 100$, where A_{SASF} is the shaded solar field area and A_{SF} is the complete

355   solar field area.

356   •   Furthermore, the shaded clear sky index S_i describes the clear sky index considering only

357   the shaded part of the solar field

358   ○ $S_i = \frac{DNI_{SASF}}{DNI_{clear}}$, where DNI_{SASF} is the average DNI within shaded areas of the solar field

359   and DNI_{clear} is the clear sky DNI.

360   Average values of the spatial DNI variability indices from the last 5 minutes are calculated. The

361   classification in one of 5 spatial DNI variability classes is done according to the thresholds given

362   in Table 2. Figure 8 illustrates a partially shaded parabolic trough solar field and the

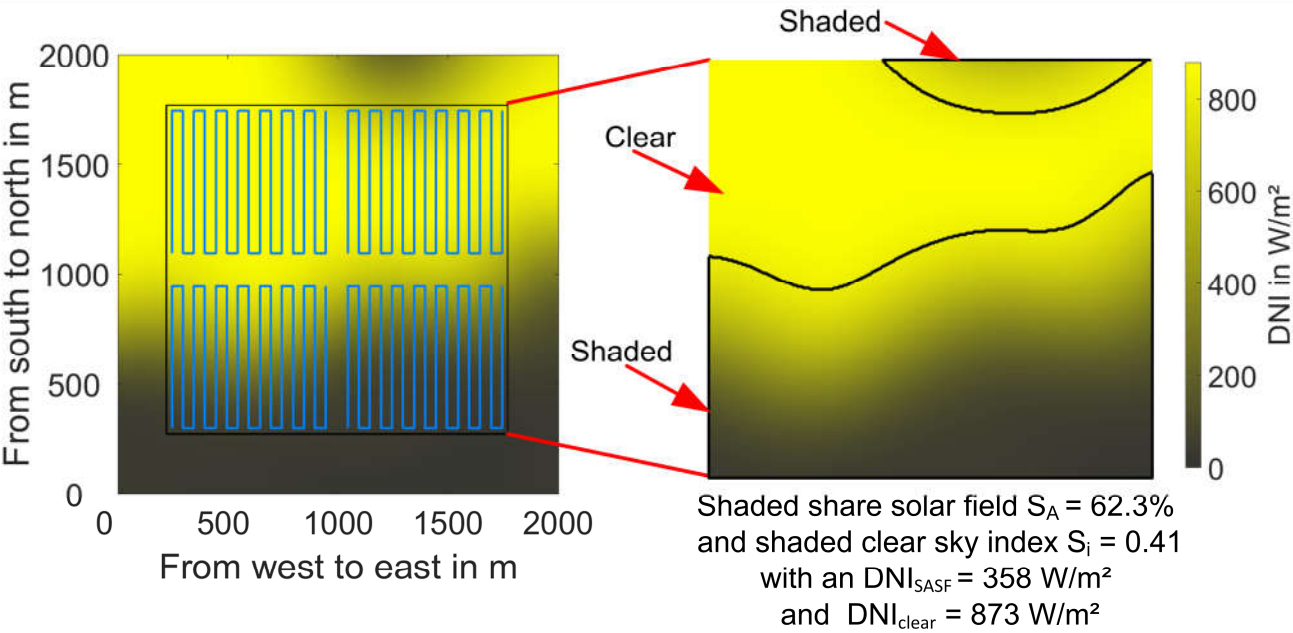363   corresponding instantaneous DNI variability indices.

364

365

Table 2: Thresholds for spatial variability classes

Class	shadow area fraction S_A [%]	Shaded clear sky index S_i	General description
1	0 – 3	no condition	Sunny conditions
2	3 – 100	0.9 – 1.0	Low spatial DNI variability: Only shadows from clouds with high transmittance
3	3 – 50	0 – 0.9	High spatial DNI variability
4	50 – 100	0.35 – 0.9	Intermediate spatial variability: Most of the solar field shaded Cases with only thin clouds and only thick clouds excluded
5	60 – 100	0 – 0.35	Low spatial variability: Most of the solar field shaded (overcast) Only shadows from clouds with low transmittance

Shaded share solar field S_A = 62.3% and shaded clear sky index S_i = 0.41 with an DNI_{SASF} = 358 W/m² and DNI_{clear} = 873 W/m²

368

Figure 8: Partially shaded solar field with a shaded share of 62.3% and a clear sky index of 0.41 corresponding to spatial DNI variability class 4

We use again the 09.09.2015 (PSA) as showcase (Figure 9). Similar to the temporal DNI variability classification, the forenoon is classified as sunny (class 1), whereas the more variable afternoon shows a stronger diversification with changing classes dominated by class 4.
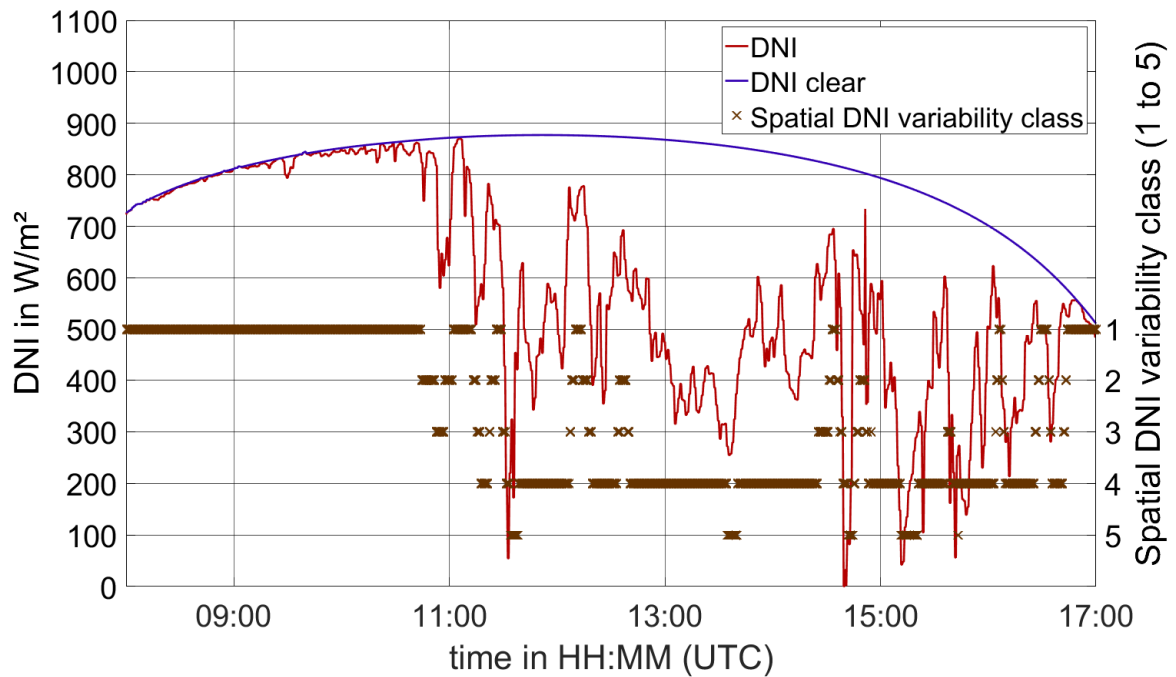
Figure 9: Spatial DNI variability classes of an example day (09.09.2015)

376 ## 4.3   Combined temporal and spatial variability classes

377 The temporal and spatial DNI variability classes describe two distinct classification approaches

378 of the DNI with different emphases. Theoretically, 40 combinations of temporal and spatial DNI

379 variability exist, but in realistic cloud situations not all combinations are likely to occur. The

380 distribution of all occurred combinations for two complete years at the PSA is depicted in Figure

381 10. The most common conditions for the PSA are described by a spatial DNI variability class 1

382 and a temporal DNI variability class 1 or 2. These clear sky conditions account for more than

383 62% of the entire data set.

384 Around 13% of the data set consists of intermediate to highly variable conditions both in time

385 and space (spatial class 3 or 4 and temporal class 3 to 7), which are the most demanding

386 situations for the parabolic trough plant control. From the view of the parabolic trough plant

387 control less important overcast conditions occur in 14.8% of the data set (spatial class 5 and

388 temporal class 6 to 8). Roughly 4% of the data set is described by a spatial class 2 and temporal

389 class 1 to 7. Such conditions with a low spatial variability but alternating temporal variability

390 occur mainly due to optical thin cirrus clouds, covering the whole power plant area as a single

391 cloud object, but having an internal spatial heterogeneity in the cloud optical depth. The

392 remaining conditions describe mainly transient conditions with an average occurrence of 0.1%

393 per combination of spatial and temporal class. Two very extreme examples are spatial class 5

394 and temporal class 1 as well as spatial class 1 and temporal class 7, with an occurrence of

395 0.29% and <0.01%, respectively. The conditions at PSA are quite attractive for a parabolic

396 trough power plant and thus relevant for the investigations carried out in this work. For the year

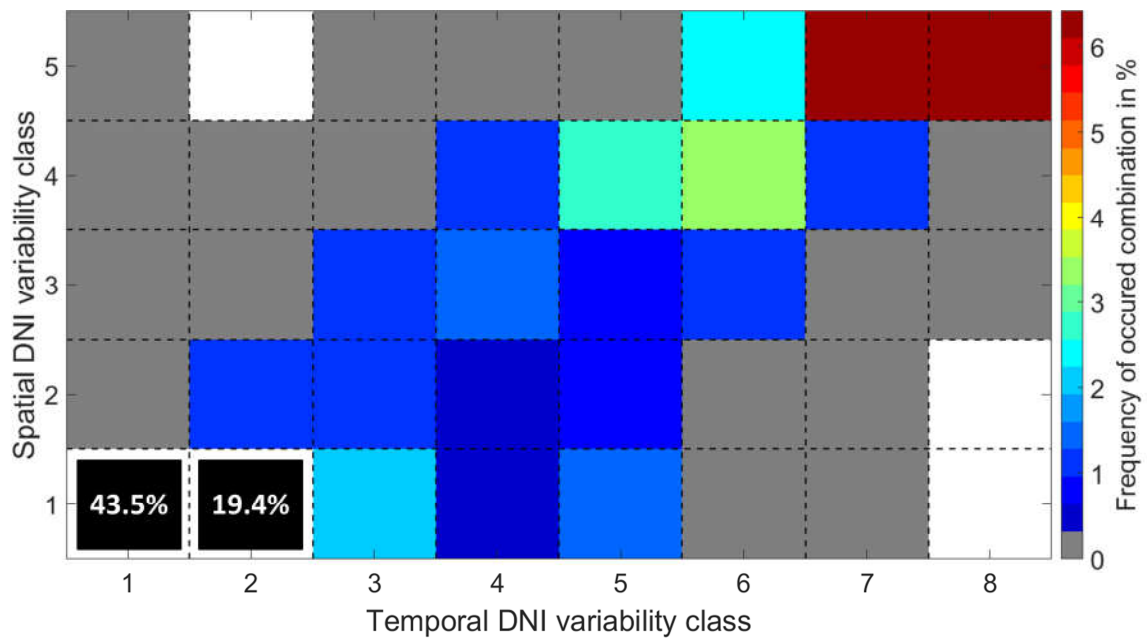397 2017 the yearly DNI sum at PSA was 2430 kWh/m².

398

399 **Figure 10: Temporal and spatial DNI variability class distribution of possible combinations within the years 2016 and**

400 **2017. Combinations of spatial class 1 & temporal classes 1 or 2 account for more than 62% of the data set. These bins**

401 **are not described by the colorbar for a better readability of the remaining combinations.**

402 Based on this assessment, the 40 possible combinations of spatial and temporal DNI variability

403 classes are combined to 7 aggregated classes according to Table 3. Due to the power plants

404 strong sensitivity on the spatial solar share, the main focus is set on the spatial variability, which

23

405   describes the distribution of the DNI over the spatially extended solar field. In cases of e.g.

406   spatial class 1, the temporal variability classification is not decisive, as all temporal classes are

407   attributed to the combined variability class 1. The temporal variability classification is relevant in

408   conditions with a strong spatial as well as temporal variability – and therefore treated separately

409   with the combined classes 6 and 7,

410   **Table 3: Combined temporal and spatial variability classes**

Combined variability class	Spatial variability class	Temporal variability class	General description
1	1	1 - 8	Sunny conditions with no spatial variability; all temporal variability classes are accepted
2	2	1 - 8	Low spatial DNI variability (almost completely sunny solar field); total spectrum of temporal variability possible
3	3	1 - 3, 5-8	High spatial DNI variability; Almost complete spectrum of temporal variability possible except highly temporal variable class 4 with an intermediate clear sky index
4	4	1 - 3, 5, 7 - 8	Intermediate spatial variability; only low and intermediate temporal variability
5	5	1 - 8	Current overcast conditions with no spatial variability; total spectrum of temporal variability possible
6	3	4	High spatial DNI variability; only highly temporal variable class 4 with an intermediate clear sky index
7	4	4 or 6	Intermediate spatial variability; only highly temporal variable classes 4 and 6

411   Looking again into our example day the 09.09.2015 (see Figure 11), we see a stronger

412   diversification within the variable time window from 10:45 to 16:45 compared to the previous

413   individual variability classifications. Whereas the purely spatial classification within this period is

414   dominated by class 4 with a share of 65% (see Figure 9), the combined class is dominated by

415   the classes 4 and 7 with a share of 36% and 29%, respectively. Both the combined classes 4

416   and 7 represent an overall intermediate spatial variability, but class 7 represents in addition a
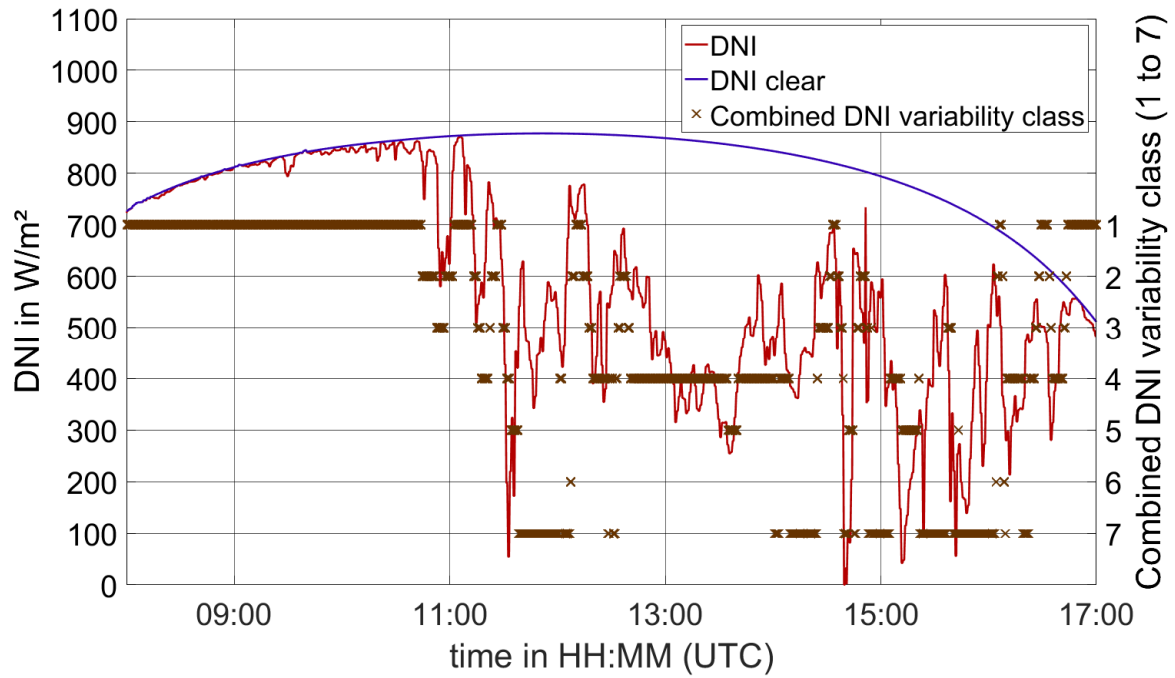
417   high variability in time.

418

Figure 11: Combined DNI variability classes of an example day (09.09.2015)

In section 5, two new solar field control strategies with optimized specific control parameters for each of the 7 combined DNI variability classes will be presented.

5 Introducing and benchmarking DNI variability class dependent solar field controllers

5.1 DNI variability class dependent solar field controllers

The solar field control system implemented in VSF is composed of local collector temperature controllers for each of the SCAs and a field main flow controller. A detailed description of the control system is published in **Noureldin et al. 2019a** and **Noureldin et al. 2019b**. In this work we present only a brief summary.

430   The local collector temperature controller regulates the HTF temperature in the receiver tubes

431   and ensures that it does not exceed the tolerated temperature limits as defined by the

432   manufactures. This is achieved by manipulating the collector angle using a proportional-integral

433   (PI) temperature feedback (FB) controller to ensure that the SCAs are tracking the sun and

434   defocusing in case the temperature set point of the SCA is exceeded. Each SCA gets an

435   individual temperature set point which is derived from the actual field inlet temperature and load.

436   In addition, there is an emergency service function, which defocuses completely the

437   corresponding SCA if the temperature limits of the HTF are exceeded.

438   Solar field outlet temperatures can be regulated by the solar field inlet mass flow. This task is

439   handled by the main solar field flow controller. The mass flow can be adjusted by the applied

440   differential pressure trough the HTF feed pump. The implemented control concept includes a

441   feed forward (FF) pump controller, a temperature feedback (FB) controller and a focus feedback

442   loop. For the FF part, the required mass flow and, thus, pump pressure is calculated by means

443   of an energy balance over the field fed by the current overall DNI. The DNI value is the average

444   of two pyrheliometer measurements as used in the real power plant (reference controller). Any

445   systematic offsets induced by the FF part are corrected by a temperature FB controller. This

446   controller uses as input the field outlet temperature set-point and operates with an adaptable

447   time constant adjusted to the throughput time of the solar field. Especially in volatile irradiance

448   situations, the large time constant of the solar field makes it challenging to avoid temperature

449   overshoots in associated loops which often trigger defocusing of one or more SCAs in the loops.

450   The focus feedback controller forces the collectors to refocus by increasing the mass flow if

451   overall defocusing states of the field increases.

452   The general form for a PI-controller for variable $u(t)$ in response to an error $e(t)$ in the process

453   variable from the set-point is

$$u(t) = K_c e(t) + \frac{K_c}{T_i} \int e(t)dt \ .$$
                                  Equation 8

454   The behavior of the local collector focus and the field main flow PI controllers can be adjusted

455   according to the first order plus dead-time method. This is achieved by deriving the controller

456   gain, K_c, and integral time, T_i, in Equation 8 from the process gain K_p, time constant T_p, process

457   dead time θ_p, such that

$$K_c = \frac{1}{K_p} \frac{T_p}{(\theta_p + \omega T_p)} \ .$$
                                    Equation 9

458   The controller gain could be further manipulated by introducing the factor ω varying from 0.1 to

459   10 for aggressive to conservative controller behavior, respectively. The integral time, T_i, is set to

460   the process time constant, T_p. The implemented reference VSF controller uses control

461   parameter as defined in Table 4 according to **Noureldin et al. 2019b**. The reference controller is

462   designed to emulate state of the art solar field control while eliminating the need for manual

463   intervention from the solar field operators. The controller has proven to work robustly in various

464   weather conditions.

465

466

467

468

469

Table 4: Process and control parameters of the reference controller according to Noureldin et al. 2019b

Controller		Parameter	Value
main flow controller	temperature feedback controller	K_p and T_p	Adaptive
		θ_p	pump pressure dependent
		K_C	aggressive
	focus feedback loop	K_p	$3\,\%/°C$
		T_p	$160\,s$
		θ_p	Simulation time step (adaptive)
		K_C	Aggressive
local SCA focus controller	temperature feedback controller (focus controller)	K_p	$-8\,°C/deg$
		T_p	$5\,s$
		θ_p	Simulation time step (adaptive)
		K_C	Moderate

471 The controller parameters presented in Table 4 are utilized as the reference case of a field

472 controller not taking into account information on spatial DNI distribution or DNI variability. In this

473 work, two new control strategies have been developed taking into account the information

474 available from the nowcasting system (spatial DNI field average and DNI variability). The

475 concept is to use different values for the controller parameters depending on the irradiance

476 situation. A clear sky situation e.g. can be operated with a more aggressive controller than a

477 strongly fluctuating situation. The adaptation of controller parameters is applied to the main flow

478 controller and to the local focus controllers. For the class dependent controller, an optimized set

479 of control parameters is defined for each of the seven combined DNI variability classes (see

480 section 4.3). The trimming of the controller parameters has been carried out for a number of test

481 situations and the parameters which best meet the criterion are selected. The first new controller

482 is trimmed to maintain the solar field outlet temperature as constant as possible whereas the

483 second one tries to maximize the solar heat collection by minimizing any defocusing. The

484 controller tuning is based on manual tuning and on the Ziegler-Nichlos method (**Schlichting**

485 **2018**). For the remaining document we will call these controllers OT (objective temperature) and

486 OFR (objective focus rate). The optimized process and control parameters are listed in Table 5

487 and Table 6. Whereas the K_p and T_p, values of the controller are pre-defined (for the focus

488 controller) or adaptively calculated for the current field situation (for the temperature FB

489 controller), the trimming is realized by modifying the tuning factor ω resulting in a conservative,

490 moderate or aggressive tuning.

491

Table 5: Adjusted process and control parameters of the class dependent controller OT

class	temperature FB controller			focus FB loop			temperature FB controller (focus controller)		
	K_p	T_p	K_C	K_p	T_p	K_C	K_p	T_p	K_C
1	adaptive	adaptive	moderate	$3\,\%/°C$	$160\,s$	Very aggressive	$-2\,°C/deg$	$50\,s$	moderate
2	adaptive	adaptive	aggressive	$3\,\%/°C$	$160\,s$	aggressive	$-2\,°C/deg$	$50\,s$	moderate
3	adaptive	adaptive	moderate	Deactivated	deactivated	deactivated	$-2\,°C/deg$	$50\,s$	aggressive
4	adaptive	adaptive	moderate	Deactivated	deactivated	deactivated	$-2\,°C/deg$	$50\,s$	aggressive
5	adaptive	adaptive	aggressive	Deactivated	deactivated	deactivated	$-2\,°C/deg$	$50\,s$	moderate
6	adaptive	adaptive	aggressive	Deactivated	deactivated	deactivated	$-2\,°C/deg$	$50\,s$	aggressive
7	adaptive	adaptive	aggressive	Deactivated	deactivated	deactivated	$-2\,°C/deg$	$50\,s$	aggressive

492

Table 6: Adjusted process and control parameters of the class dependent controller OFR

class	temperature FB controller			focus FB loop			temperature FB controller (focus controller)		
	K_p	T_p	K_C	K_p	T_p	K_C	K_p	T_p	K_C
1	adaptive	adaptive	moderate	$3\,\%/°C$	$160\,s$	Very aggressive	$-6\,°C/deg$	$115\,s$	moderate
2	adaptive	adaptive	aggressive	$3\,\%/°C$	$160\,s$	aggressive	$-6\,°C/deg$	$115\,s$	moderate
3	adaptive	adaptive	conservative	deactivated	deactivated	deactivated	$-6\,°C/deg$	$115\,s$	moderate
4	adaptive	adaptive	moderate	$3\,\%/°C$	$160\,s$	moderate	$-6\,°C/deg$	$115\,s$	moderate
5	adaptive	adaptive	conservative	$3\,\%/°C$	$160\,s$	moderate	$-6\,°C/deg$	$115\,s$	moderate
6	adaptive	adaptive	aggressive	deactivated	deactivated	deactivated	$-6\,°C/deg$	$115\,s$	moderate
7	adaptive	adaptive	aggressive	deactivated	deactivated	deactivated	$-6\,°C/deg$	$115\,s$	moderate

493 ## 5.2 Selection of assessment days

494 The benchmark is performed over 22 days distributed over the year 2015 at PSA. The data set

495 is chosen in such a way, that it includes a wide variety of conditions in irradiance, cloud height

496 and type (low layer, middle layer, high layer and multi-layer conditions) as well as the resulting

497 DNI variability classes (see Figure 12). The cloud height information is shown since it is one of

498 the main uncertainty contributors of ASI systems (**Nouri et al. 2019b; Nouri et al. 2019c**). Cloud

499 height measurements are taken by a CHM 15 k Nimbus ceilometer from G. Lufft Mess- und
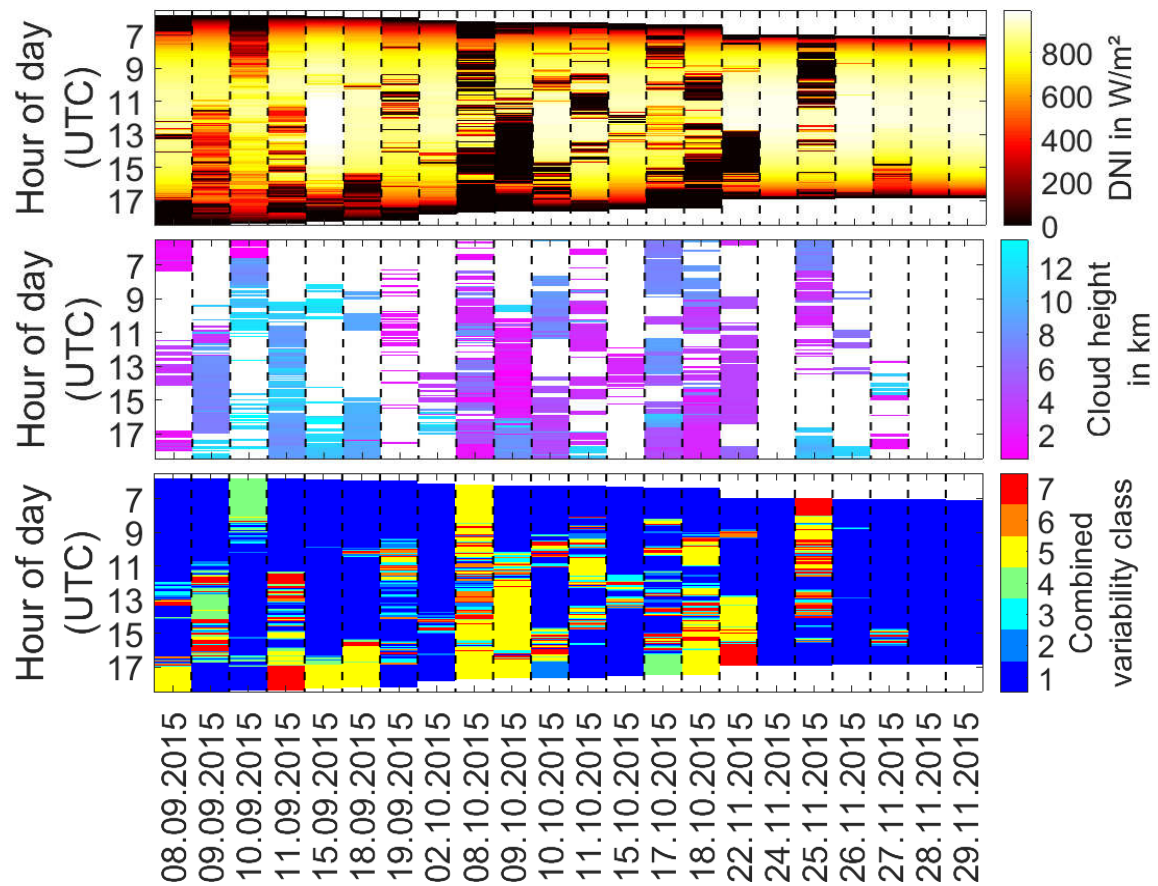
500 Regeltechnik GmbH.

501

Figure 12: Pyrheliometer based DNI, cloud height as measured by a ceilometer and combined DNI variability class over the 22 test days

Comparing the distribution in combinations of spatial and temporal DNI variability class during the 22 test days (see Figure 13), it reveals that the 22 days include almost all combinations of the 2 year period as analyzed in section 4.3. Only 6 combinations which exist in the two year period are missing in the 22 days test period. These 6 combinations describe rather rare transient conditions which make less than 0.37% of the entire 2 year data set. Overall the 22 days include with 19.2% a higher share of the intermediate to highly variable conditions (spatial class 3 or 4 and temporal class 3 to 7), compared to 13% in the 2 year data set. In turn, less interesting overcast conditions (spatial class 5 and temporal class 6 to 8) have only a share of 7.8% compared to 14.8% within the 2 years. For the remaining combinations the 22 days resemble the two year data set very well.
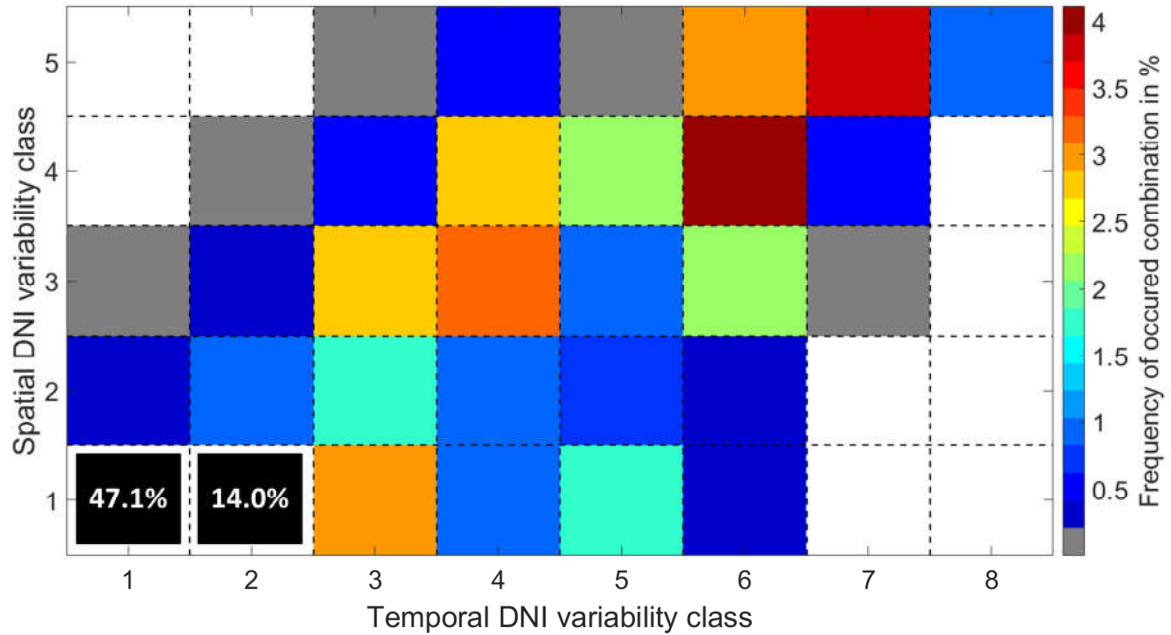
30

Figure 13: Temporal and spatial DNI variability class distribution of possible combinations within 22 test days. Combinations spatial class 1 & temporal classes 1 or 2 account for more than 61% of the data set. These bins are not described by the colorbar for a better readability of the remaining combinations.

5.3   Comparison with a state of the art reference controller

In this section the two new class dependent solar field controllers are benchmarked against the state of the art reference controller based on the La Africana power plant design. Five different criteria are used to evaluate the solar field controller's performance.

- Overall expected revenues in € between the new class dependent controller and the reference controller.
- The accumulated solar field thermal heat flow
- Average solar field focus rate as relative value. It accounts to 100%, if all collectors of the solar field are fully focused.
- RMSD of the solar field outlet temperature with the design set temperature as reference.

31

528 • Reduction of emergency defocus incidents: Relative value which compares whether or

529 not the new class dependent controller is capable of reducing emergency defocus

530 incidents with respect to the reference controller. Emergency defocus incidents occur

531 when the fluid temperature exceeds a maximum safety threshold indicated by the fluid

532 manufacturer.

533 The revenue is considered as the decisive parameter for the evaluation of the controller

534 performance. The other parameters contribute to a better understanding of the controller's

535 individual behavior. The spider plot in Figure 14 illustrates the overall results for these five

536 criteria. Only relative changes to the reference controller are depicted, where positive values

537 indicate an improvement and negative values a decline in performance in a particular criteria.

538 For example, the calculation of change in relative revenue is always calculated according to

539 Equation 10

$$c_{rel.rev} = (rev_{classDep}/rev_{ref} - 1) \cdot 100\%$$

Equation 10

540 ,where rev_{ref} is the revenue of the reference controller and $rev_{classDep}$ is the corresponding

541 revenue of the class dependent controller.

542 The class dependent controller OT outperforms the reference controller in all criteria. In terms of

543 overall revenue, the controller OT outperforms the reference controller by 1.38%.

544 A particularly significant improvement can be seen by the controller OT for the criteria reduction

545 of emergency defocus incidents with 18.6%. Emergency defocus incidents can lead to strong

546 temperature transients within collectors (temperature gradients above 40°C in 3 minutes are

547 possible), which affect the overall system stability, solar field outlet temperature and focus rate.

548 This reduction of emergency defocus incidents by itself is already an important improvement.

549   Emergency defocus incidents are triggered by exceeding maximum safety threshold

550   temperatures within the collectors. The emergency defocus means first of all that additional

551   operations of the collector drives and rotation and expansion performing assemblies (REPA) are

552   necessary, which could accelerate degrading effects. Furthermore, frequent temperature

553   transients, especially with temperatures by several degrees above the set point, could affect the

554   lifetime of REPAs, HTFs, receiver tubes and all other components exposed to the transients.

555   Since sufficient experience on the degradation mechanisms is not yet available, the findings

556   cannot be directly translated into economic figures.

557   The class dependent controller OFR reaches a revenue increase of 1.40%, nearly identical to

558   the increase for OT. However, while OFR also outperforms the reference in focus rate and heat

559   flow, it is outperformed by the reference in terms of RMSD temperature (by -5.4%) and

560   emergency defocus incidents (by -0.6%). Despite the objective of this controller it performs only

561   marginally better than the controller OT in focus rate with an improvement of 1.62% compared to

562   an improvement of 1.48%. This can be partly explained by the significantly higher number of

563   emergency defocus incidents compared to the controller OT. Each emergency defocus incident

564   leads to a short-term total defocusing of a collector and in turn to additional temperature

565   transients which is reflected by the increased RMSD. This leads to a stronger penalization of the

566   controller OFR compared to the controller OT and thus to a similar improvement in revenue,

567   despite the higher overall heat flow for OFR. Increased number of incidents is caused by the

568   target of the controller. The higher number of emergency defocus incidents is caused by the

569   controller OFR objective. In order to keep the focus rate as high as possible, the controller OFR

570   uses predominantly the pump pressure as control variable, intending to adapt the mass flow to

571   the prevailing conditions while maintaining a constant high focus rate. This approach usually

572   leads to a higher heat flow, yet, it is more vulnerable under variable quickly changing conditions

33

573   in which adaptation of the focus rate are inevitable. A partially too late intervention of the local

574   SCA focus controller gives less leeway for countermeasures, which in turn leads to a higher rate

575   of emergency defocus incidents.
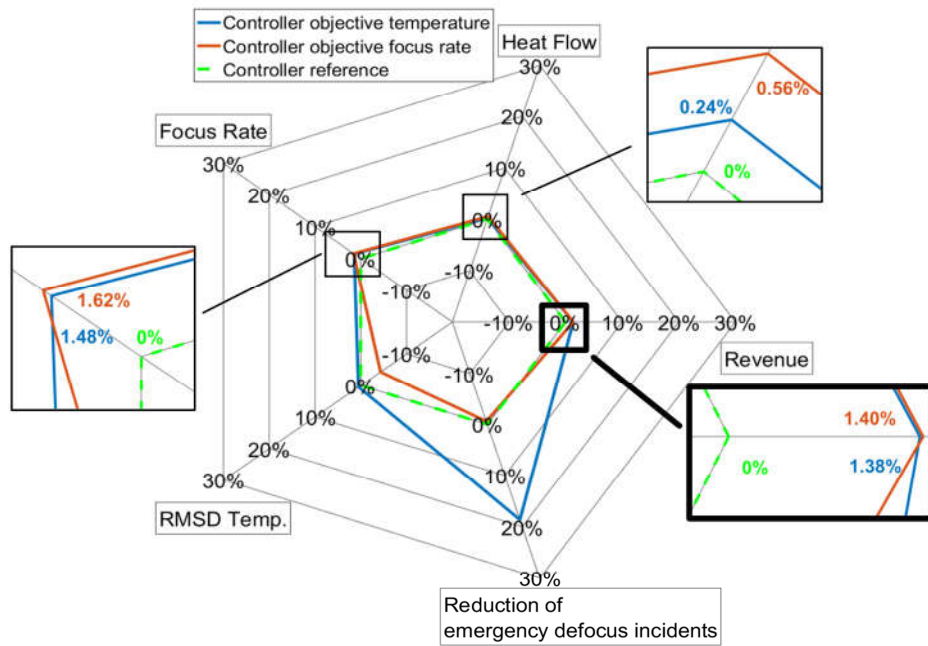
576

577   **Figure 14: Comparison of the three controller setups reference, objective temperature, objective focus rate over 5**

578   **criteria and based on 22 test days. Relative changes compared to the reference controller are plotted. Positive values**

579   **indicate an improvement and negative values a decline in performance in a particular criterion.**

580   For each day, the absolute revenue and the change of relative revenue between the reference

581   controller and the two class dependent controller are compared in Figure 15. Both class

582   dependent controllers outperform the reference controller in 20 out of 22 days. The

583   underperforming days are characterized by longer time periods with fast changing variability

584   classes (see Figure 12). How such an underperformance can be avoided is discussed in the

585   next section.

586   It is observed that the potential gains in revenue are rather different between all days. The

587   lowest revenue is expected on the 25.11.2015 with roughly 7.9 k€ (reference control) and the

588 highest on the 15.09.2015 with roughly 98.8 k€ (reference control). Over all 22 days the absolute

589 benefit of the new class dependent controller amounts to roughly 15 k€ for the controller OT and

590 roughly 15.2 k€ for the controller OFR with an overall absolute revenue of roughly 1,083.3 k€

591 (reference controller). This is an increase of about 1.4 % in revenue for the new class dependent
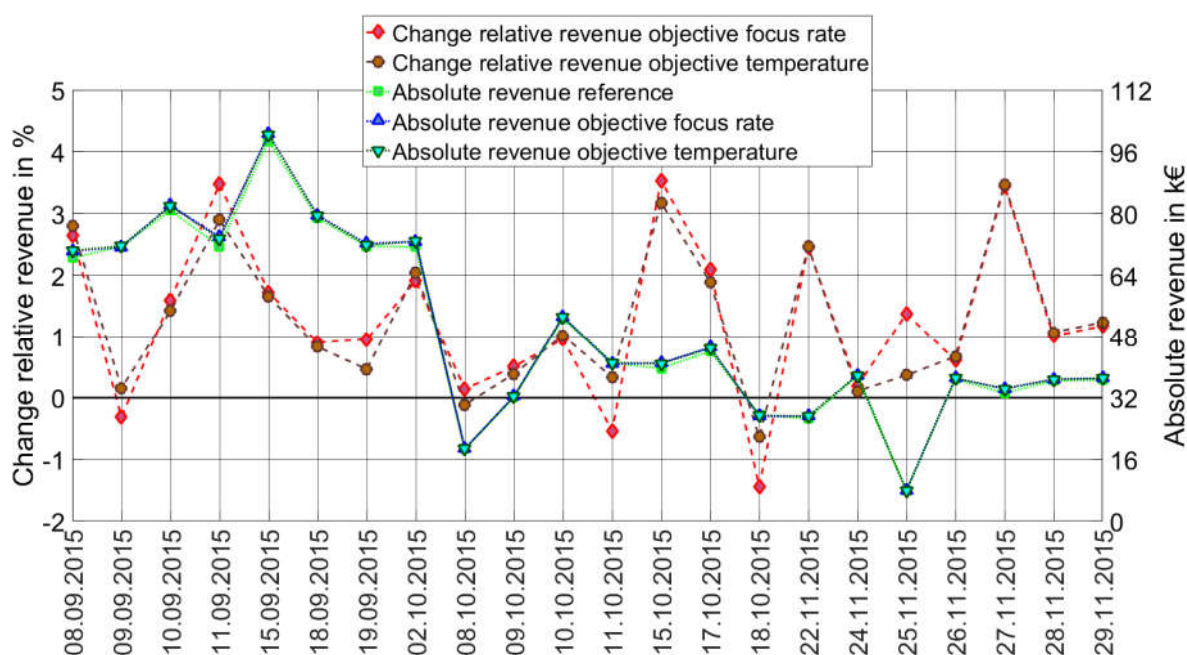
592 controller concept.

593

594 **Figure 15: Absolute and relative daily revenue for reference controller and the two class dependent controllers.**

595 # 6 Detailed performance assessment and applicability conditions

596 ## 6.1 Identification of applicability conditions

597 In section 5.3 we investigated the benefit of the class dependent controller compared to the

598 reference controller. These analyses looked at the overall benefit over the entire data set or over

599 complete days. A clear benefit is visible in terms of revenue. Yet, it might be the case that the

600 class dependent controller will be outperformed by the reference controller under certain

601 conditions.

602   In this section, we discretize the entire data set into short data packages and analyze the impact

603   of the combined DNI variability classes as well as the combinations of spatial and temporal DNI

604   variability classes on the expected revenue. The goal is to identify a binary decision system,

605   which will decide if either a class dependent controller or the reference controller is preferable

606   for the prevailing conditions. We call this binary decision system as the identification of

607   applicability of the ASI derived DNI variability class and the enhanced controller.

608   A DNI variability classification update is performed every 30 s, according to the ASI system

609   resolution. The spatial DNI variability classification uses information of the past 5 minutes and

610   the temporal classification of the past 15 minutes. For the identification of applicability

611   conditions, we discretize the 22 days in sliding data packages of 10 minutes duration. The

612   resolution of these sliding data packages corresponds to the temporal resolution of the ASI

613   system of 30 seconds. Each data package time stamp corresponds to the end of the package.

614   The 22 days result in roughly 20000 data packages. These data packages enable a high

615   temporal resolution impact analysis of the actual DNI variability classes on the controllers. No

616   aggregation over the data packages is done. An aggregation would lead to an artificial repetition

617   of the same time stamps within the summed up values.

618   Considering the solar field time constant of approximately 10 min, it is obvious that 10 minute

619   data packages might be too short to fully cover some of the processes which unfold more slowly

620   within some parts of the extensive solar field. This leads to the situation that a certain analysis

621   window is not only affected by the DNI situation during this time window but also from the DNI

622   situation and the controller activity in the previous time periods. Especially when DNI classes

623   rapidly change along the analysis windows, exist no one to one mapping of classification to

624   controller result. Nevertheless, the used 10 minute time windows cover many occurring

625 processes. Longer time windows would corrupt the intention of this analysis, since they would

626 again average out effects we want to work out.

627 In section 6.2 we will present the benefit of the applicability conditions according to the results

628 presented in section 5.3 without the discretization in sliding data packages.

629 The change in relative revenue of all data packages is discretized and averaged within the

630 combined DNI variability classes (see Figure 16). The combined class 1 describes the dominant

631 sunny conditions within the data set with an occurrence of 67%. The controller OT shows an

632 advantage compared to the reference controller for the classes 1, 2, 6 and 7 which account for

633 more than 82% of the data set. The controller shows a significant disadvantage during combined

634 class 4 conditions, which describe an intermediate spatial variability with a low to intermediate

635 temporal variability. Under these conditions, more than 50% of the solar field is shaded.

636 The controller OFR shows an even stronger advantage compared to the reference controller for

637 the classes 1, 2, 6 and 7 as well as class 3 which account together for more than 88% of the

638 data set. However, the class 4 and 5 show a very pronounced disadvantage in revenues

639 compared to the reference. The absolute energetic loss for these classes is comparably low,

640 since these classes are rare and as they have a high shaded solar field share and a low cloud

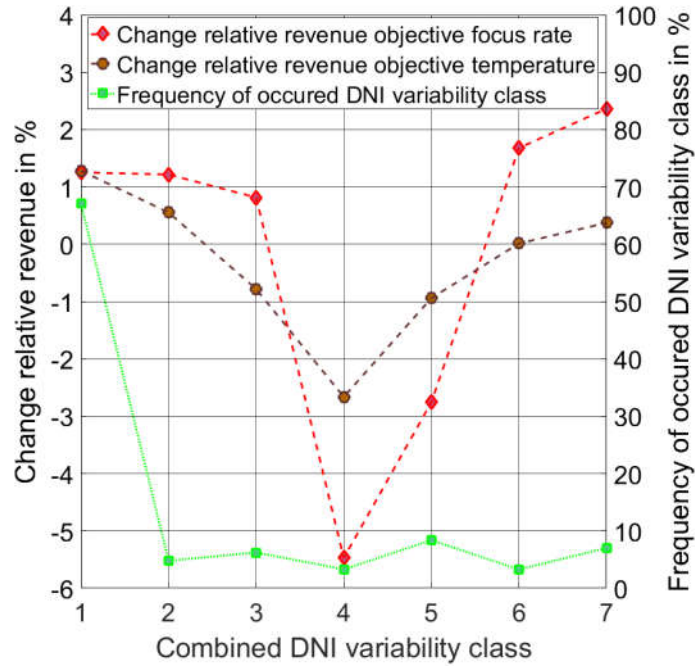641 transmittance (especially for class 5).

Figure 16: Change relative revenue discretized over combined variability classes and occurrence of classes within the complete data set

Most of the combined DNI variability classes (with exception of combined class 6) include more than one combination of spatial and temporal DNI variability classes. Therefore, we discretized the change in relative revenue of all data packages in the combinations of spatial and temporal DNI variability class. The results of this analysis are shown in Figure 17, which considers the spatial class on the y axis, the temporal class on the x axis, the change in relative revenue by the color coding and the occurrence of a certain conditions as the stated value within the bins.

The class dependent controllers outperform the reference controller in 20 (OT) and 22 (OFR) combinations of spatial and temporal DNI variability conditions (green and cyan bins). They are outperformed in 11 (OT) and 9 (OFR) combinations (red and purple bins), of which 6 are identical for both controllers. The mentioned 20 and 22 combinations of spatial and temporal DNI variability classes account for more than 85% (OT) and 89% (OFR) of the data set. Almost all conditions with an advantage for the reference controller are found for highly variable

657 conditions, which are connected to a low average DNI and plant yield. For each class dependent

658 controller only one underperforming combination of spatial and temporal DNI variability class is

659 found, which can be connected to a high average DNI and yield. However, these combinations

660 account for less than 0.3% of the data set.

661 The combination of spatial class 5 and temporal class 3 shows for both controllers a change in

662 relative revenue above 20%. On the contrary, the combination of spatial class 3 and temporal

663 class 7 shows for both controllers a change in relative revenue around -20%. However, both

664 these combination account for less than 0.1% of the data set and are therefore mostly irrelevant.

665 For the remaining combinations the change in relative revenue is clearly within ±10% (mostly

666 ±5%).

667 The results depicted in Figure 17 are utilized for the identification of the applicability of the class-

668 dependent controller. For each combination of spatial and temporal DNI variability class with an

669 expected benefit in revenue, it makes sense to use the class dependent controller whereas the

670 reference controller is recommended for the remaining combinations. Thus, this matrix defines

671 the applicability of the class dependent controller giving the name to the overall concept of

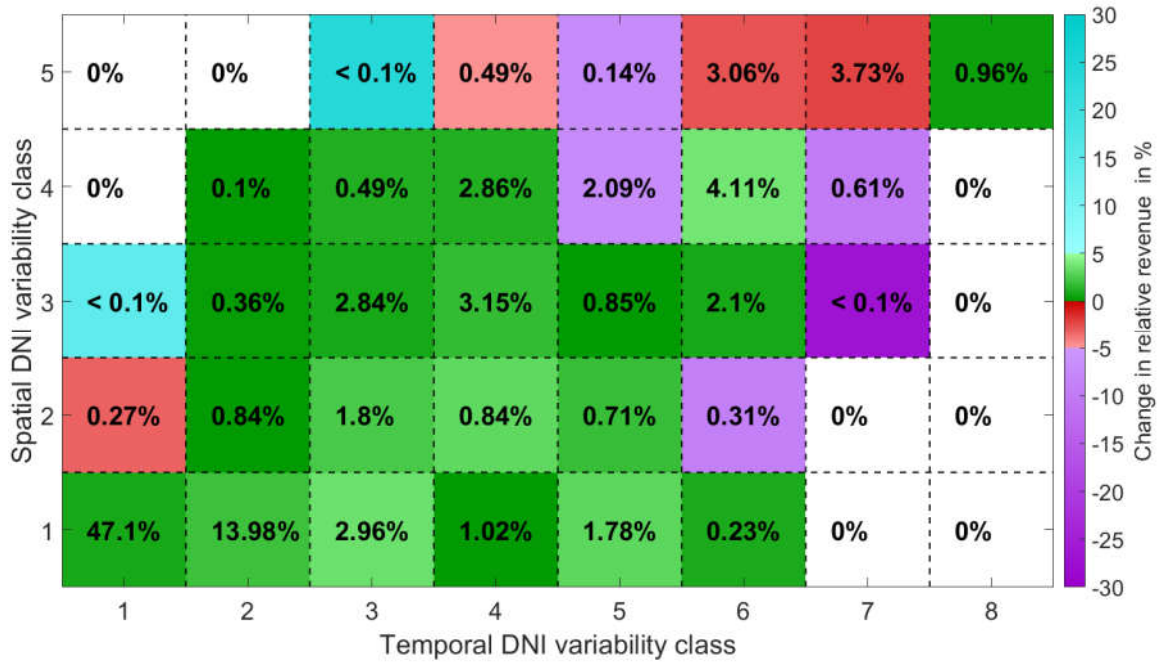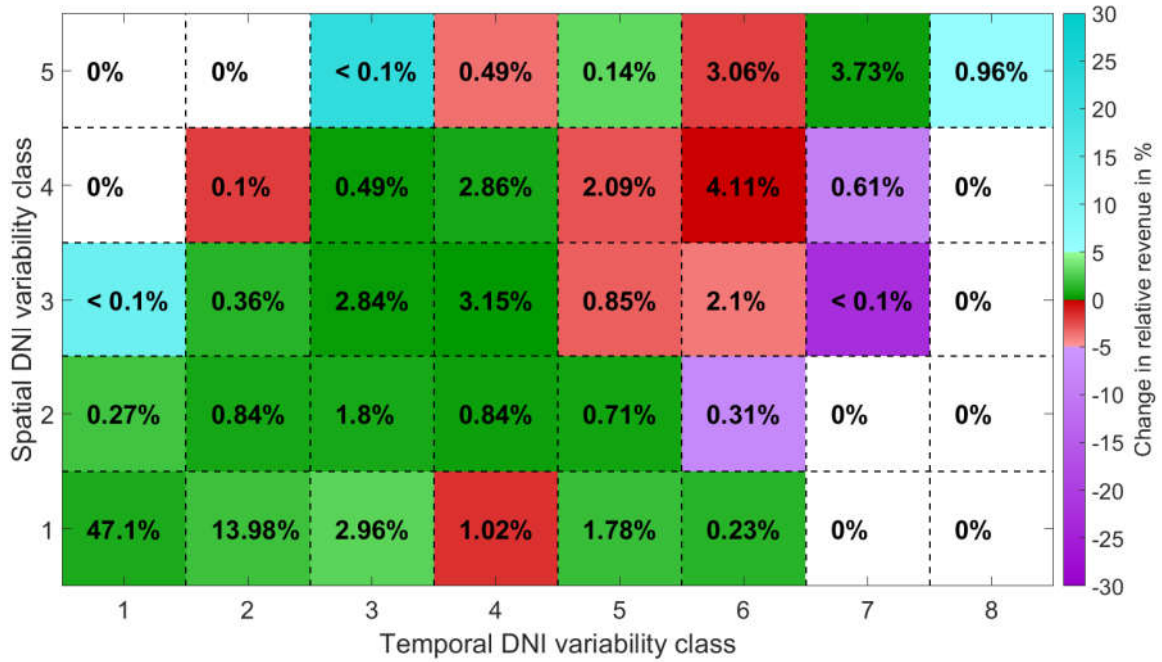672 applicability classes for the solar field control.

673

674

675

676 **Figure 17: Change in relative revenue discretized in combinations of temporal and spatial DNI variability classes. The**
677 **color coding describes the relative change in revenue within each bin. The occurrence of each bin is indicated by the**
678 **stated values. (top) controller OT (bottom) controller OFR**

679 ## 6.2 Using applicability identification for the plant control

680 In this section we describe how the above findings can be used to create an improved

681 hybridized control strategy. The hybridized control concept consists of two sets of controllers.

682   The first one is the reference controller making use of the irradiance information from the two

683   pyrheliometers whereas the second one uses the class dependent control parameters and

684   additional information from the ASI system. The ASI information delivers the DNI average over

685   the field as well as the classification into temporal and spatial DNI classes. The applicability

686   matrix defined in the last section is used to decide whether the reference controller or the class

687   dependent controller is used in the current DNI situation represented by the class derived from

688   the ASI information.

689   All 22 days are evaluated once again with the VSF using this hybridized control strategy for both

690   class dependent controllers. We will continue to call the hybridized controller class dependent

691   controller with the objective temperature (OT) and focus rate (OFR), since for the hybrid

692   operation the class dependent controller account for the predominant share of the data set.

693   Compared to the analysis presented in section 6.1, the applied controller is now continuously

694   selected based on the class whereas in the former study the same controller was used

695   throughout the day only adapting its parameters according to the prevailing class. In a first step,

696   we analyze the performance based on the 10 min sliding data packages according to section

697   6.1. The improvement due to the class dependent controllers with regards to the applicability

698   conditions is evident, when looking into the overall change in relative revenue discretized over

699   the combined temporal and spatial DNI variability classes (see Figure 18). The controller OT

700   shows a significant increase especially for the classes 2, 3, 4, 6 and 7. This holds especially for

701   class 4 where the relative revenue changes from a decrease of -2.7% to an increase of 4.6%.

702   Nonetheless, we see also a slight decrease for class 5. The controller OFR shows a significant

703   increase within all classes. For class 4 and 5, the previous reductions of -5.5% and -2.8% in

704   revenues increase to 5.1% and 3.5%, respectively.
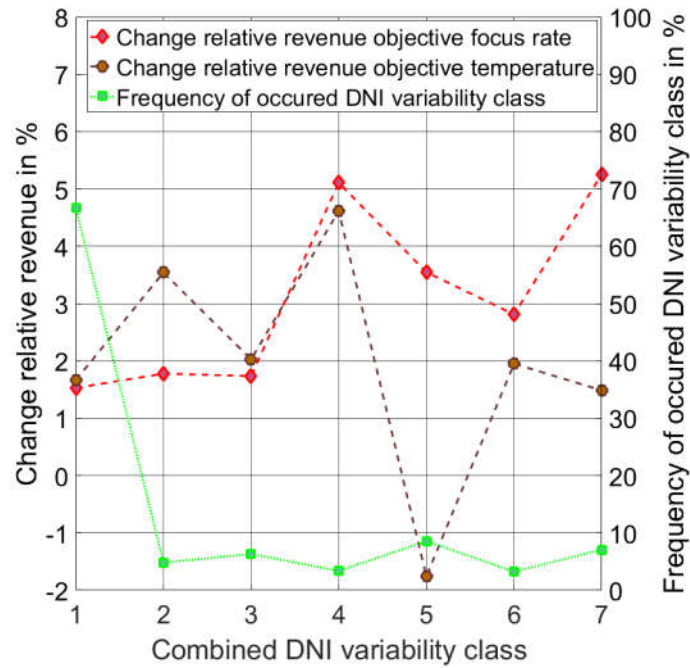

41

Figure 18: Change relative revenue discretized over combined variability classes and occurrence of classes within the complete data set (hybridized controllers with regards to the applicability conditions)

Looking into the change in relative revenue discretized over the combinations of spatial and temporal DNI variability classes, we observe that both class dependent controllers outperform the reference controller in 25 combinations. They are only outperformed in 6 combinations, which account for 9% (OT) and 3.2% (OFR) of the data set (see Figure 19). Four of these six unfavorable combinations are identical for both controllers. The considerable higher share in the case of controller OT is due to the two combinations spatial 5 and temporal 6 and 7. Each of these combinations has a share above 3% of the data set. Overall, the absolute energetic effect of these combinations is insignificant as they refer to almost fully shaded low DNI conditions. These two combinations also explain the slightly negative impact in combined DNI variability class 5 on the controller OT (see Figure 18).
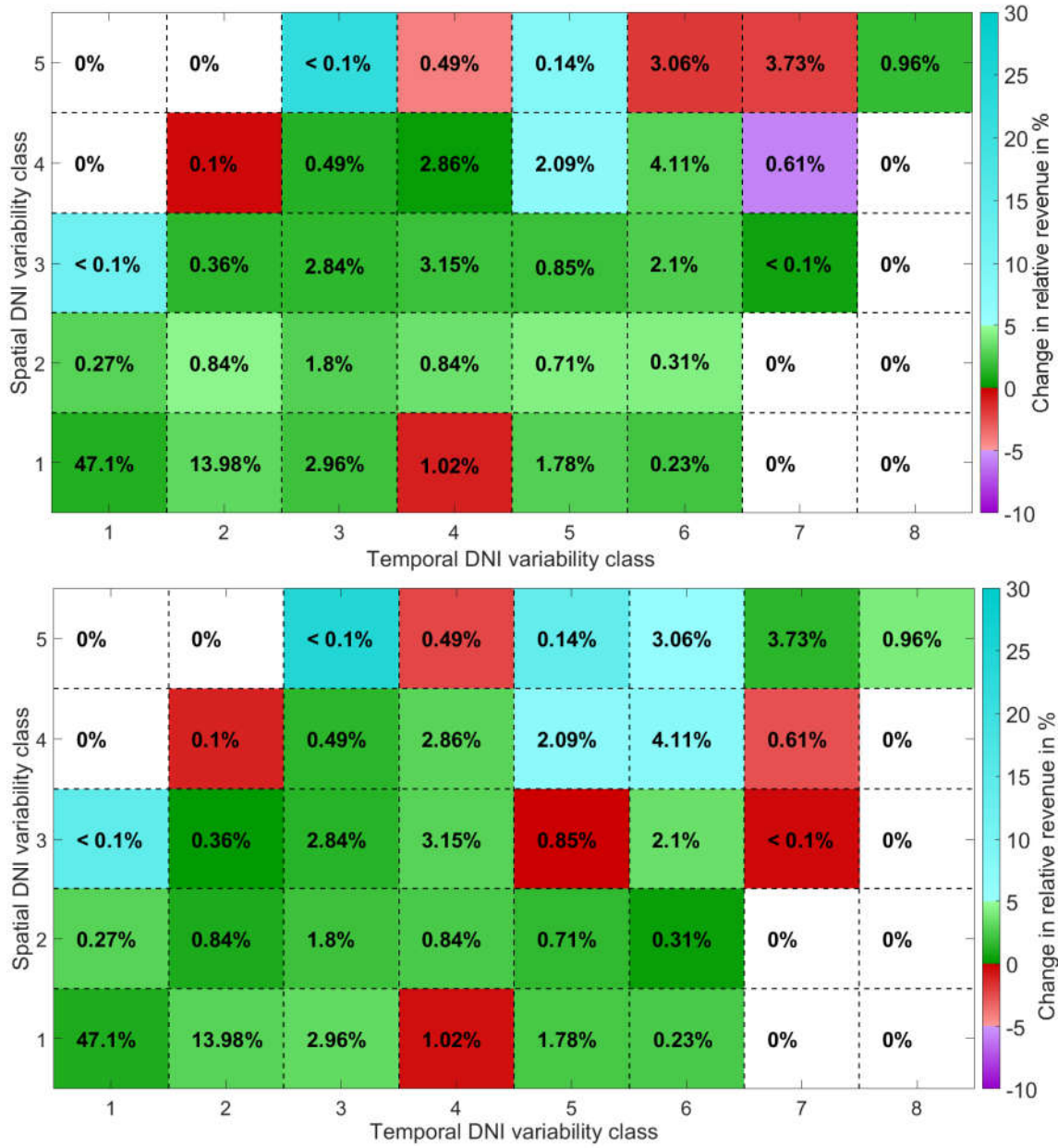
718

719

720   **Figure 19: Change in relative revenue discretized in combinations of temporal and spatial DNI variability classes for**

721   **hybridized controllers using the applicability. The color coding describes the relative change in revenue within each**

722   **bin. The occurrence of each bin is indicated by the stated values. (top) hybridized controller OT using the identified**

723   **applicability (bottom) hybridized controller OFR using the identified applicability**

724   In a next step we analyze the impact of the applicability conditions on the overall results

725   according to section 5.3, without the discretization of sliding data packages in DNI variability

726   classes. Figure 20 shows the change in relative and absolute revenues discretized over the 22

727   days. Both class dependent controllers show a significant improvement compared to the results

728   presented in section 5.3. The overall absolute revenue compared to the reference controller

729   rises by roughly 20.9 k€ (OT) and roughly 21.2 k€ (OFR) with the hybridized concept. Without

730   the continuous selection between reference and class dependent controller these improvements

731   were considerably lower with roughly 15 k€ (OT) and 15.2 k€ (OFR). For the hybrid concept, the

732   reference controller outperforms the controller OT only on the 08.10.2015 and the controller

733   OFR on the 25.11.2015. These days with roughly 18.7 k€ (08.10.2015 reference controller) and

734   7.9 k€ (25.11.2015 reference controller) have the lowest overall absolute daily revenue. On

735   08.10.2015, the combined variability class 5 accounts for 57% of the day (see Figure 12). As we

736   see in Figure 18, the reference controller outperforms the class dependent controller OT by

737   roughly 1.8% within the combined DNI variability class 5. Therefore, it is not surprising that the

738   reference controller outperforms the controller OT on this day. The 25.11.2015 is a highly

739   complex day with multi-layer cloud conditions (see Figure 12). This day is responsible for 27% of

740   all emergency defocus incidents (reference controller) during the 22 days. As we discussed in

741   section 5.3, the controller OFR is much more vulnerable for emergency defocus incidents

742   compared to the controller OT. This explains the strong deviation in revenue change from +8.8%

743   (OT) to -2.1% (OFR). Concerning the high fluctuations of the relative values, it should not be

744   forgotten that this day accounts to an absolute revenue of only 7.9 k€ (reference controller).
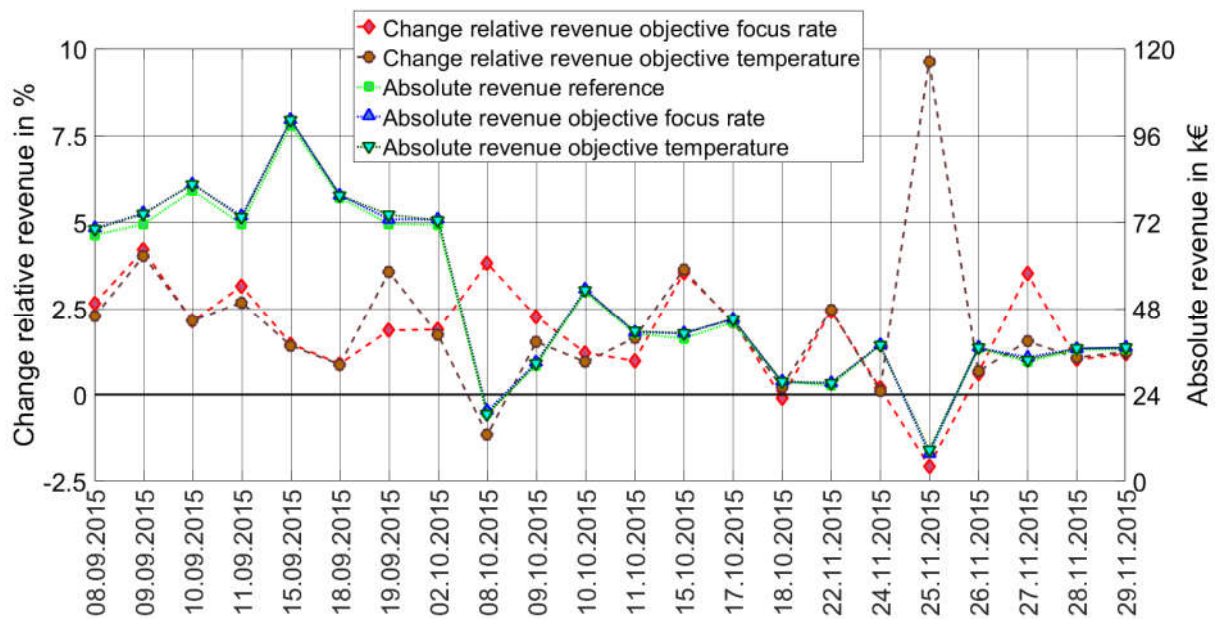
745

Figure 20: Absolute and relative daily revenue for the reference controller and the two hybridized class dependent controllers with regards to the applicability conditions

Figure 21 illustrates the overall influence of the controllers with regards to the applicability conditions over the previously introduced five criteria. The class dependent controllers outperform the reference controller in all criteria. The advantages and disadvantages of both class dependent controllers are almost completely balanced in terms of revenue, with a benefit above 1.9% for both class dependent controllers compared to the reference controller. Especially the controller OT shows a significant improvement in the criteria RMSD temperature and reduction of emergency incidents by 9.5% and 21%, respectively. The controller OFR outperforms the controller OT in terms of heat flow, focus rate and revenue.
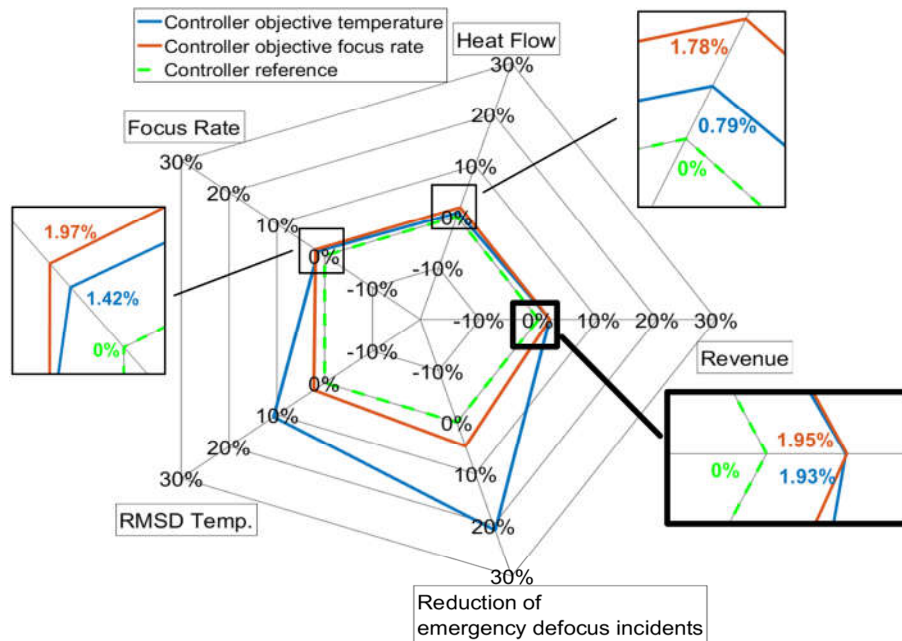
Figure 21: Comparison of hybridized class dependent controllers using applicability against the reference controller 5 criteria and 22 days. Relative changes compared to the reference controller are plotted. Positive values indicate an improvement and negative values a decline in performance in a particular criterion.

7 Conclusion

We developed a combined temporal and spatial DNI variability classification consisting of 7 distinct classes that allows an improved control of parabolic trough power plants. This combined classification procedure includes a temporal DNI variability classification with eight distinct classes as well as a spatial DNI variability classification with 5 distinct classes. Spatial DNI information, provided by an ASI system, are used for the spatial DNI variability classification.

Three set ups of controller parameters have been defined based on the same underlying control concept. The reference controller is used as the basis for two modified controller setups. The reference controller parameters for these two additional controllers are trimmed in a way to result in more aggressive or conservative behavior of the controller. Individual trimming values are used for each of the combined DNI variability classes. The two trimmed controller

772   configurations differ in their behavior. The first has a trend to strongly improve stability the field

773   outlet temperature (called objective temperature, OT) whereas the second tends to increase the

774   overall focusing rate of the field (called objective focus rate, OFR). These new controllers are

775   tailored for a parabolic trough solar field design according to the La Africana 50MW power plant.

776   A benchmark over selected 22 days with variable DNI and different cloud conditions has been

777   performed representing a wide variety of irradiance conditions. The chosen 22 days match the

778   distribution of DNI variability conditions found at PSA over two complete years helping to

779   generate representative results for real situations.

780   The reference controller considers a state of the art solar field controller with DNI information

781   from two pyrheliometers as typically available ground observations in commercial power plants

782   as e.g. the La Africana power plant in Spain. The DNI information is used in a feedforward loop

783   to calculate the expected mass flow required for the actual irradiance. The two other controllers

784   do not use the two meteo station signals but refer to the average DNI values calculated from the

785   DNI map delivered by the ASI system.

786   In the performance assessment study, the actual ruling DNI conditions acting on the solar field

787   are provided by a separate nowcasting system based on shadow cameras, which are looking

788   from above on the same area. These shadow cameras are providing an independent and more

789   accurate estimate of the spatial distribution of DNI. Thanks to the solar towers available at the

790   PSA, this unique assessment opportunity is available, while in commercial parabolic trough

791   power plants most likely only the ASI based spatial DNI information will be available.

792   Five different economical and technical performance criteria are compared: the total solar field

793   thermal heat flow, solar field focus rate, RMSD of the solar field outlet temperature (design set

794   temperature as reference), reduction of emergency defocus incidents, and revenue. In terms of

795 revenue, the major economic criterion, both class dependent controllers are found to be quite

796 similar, despite the higher heat flow of the controller OFR. OFR outperforms the reference by

797 1.40% and OT by 1.38% if aggregated over the entire 22 day data set.

798 The controller OT outperforms the reference also in the remaining 4 technical performance

799 criteria. In comparison, the controller OFR outperforms the reference controller in focus rate and

800 heat flow, but is outperformed in RMSD of the solar field outlet temperature and reduction of

801 emergency defocus incidents by the reference controller. This explains the close match in

802 revenue between OFR and OT. The higher RMSD of the solar field outlet temperature translates

803 in a higher volatility of the outlet temperature as well as the associated higher number of

804 emergency defocus incidents, which is considered by the revenue calculation trough the

805 penalties.

806 In a subsequent more detailed evaluation step, we evaluated under which conditions the new

807 controllers lead to a revenue increase and whether there exist situations causing a revenue

808 decrease. Increasing revenue conditions are considered as applicable, while the aim is to detect

809 the unfavorable conditions in real time and to avoid using the new controller in such situations.

810 For this evaluation, we discretized the 22 days in 10 minutes sliding data packages.

811 Furthermore, each of these data packets was discretized to one of 40 theoretically possible

812 combinations of spatial and temporal DNI variability classes. The overall relative change in

813 revenue within each combination was analyzed. Around 85% (OT) and 89% (OFR) of the data

814 set turned out to be applicable for the new controller.

815 Finally, a hybridized control strategy with regards of the applicability conditions was investigated.

816 Whenever applicable conditions are present, the variability class dependent controllers with DNI

817 maps are utilized. Otherwise, only the DNI information from two pyrheliometers as input to the

818 reference controller is used.

819 The results of the hybridized control strategy are promising. Both hybridized class dependent

820 controller setups outperform the reference controller in all 5 criteria. In terms of revenue, the

821 reference controller is outperformed by 1.93% (OT hybridized) and 1.95% (OFR hybridized),

822 over the entire data set.

823 A significant reduction of emergency defocus incidents (21%) is visible for the controller OT

824 (hybridized). This could lead to an additional reduction of maintenance costs, as emergency

825 defocus incidents are related to strong fluctuation in temperature as well as temperatures above

826 safety thresholds, affecting various components within the solar field but also balance of plant.

827 However, these effects cannot be quantified until now.

828 The expected additional absolute benefit in revenue increases to roughly 20.9 k€ (OT

829 hybridized) and roughly 21.2 k€ (OFR hybridized), over the 22 test days compared to the

830 reference controller.

831 Finally, we conclude that there are significant possibilities to improve the solar field controller of

832 parabolic trough power plants with spatial irradiance information from ASI systems, despite the

833 uncertainties. The variability classification procedure is a crucial element of the concept and

834 reveals the critical information in a suitable manner as needed by the controller. The

835 classification procedure is a substantial requirement to realize the revenue increase, since

836 situation dependent control parameters can be used. The uncertainties of the spatial DNI

837 information might be considerably high at any given moment and for any discrete spot of the

838 solar field. Yet, the ASI system appears to be capable to catch the prevailing overall spatial and

839 temporal DNI variability conditions accurately enough for the plant control. Overall, it is the

840 classification procedure which uncovers the relevant characteristics of DNI in a proper manner.

841 This became apparent in initial preliminary studies, where the solar field controller had access to

842 the spatial DNI field average from the ASI system, but without the DNI variability classification

843 and the corresponding controller adaptations. Only a slight benefit of few tenth percent in

844 revenue compared to the reference controller were observed in these initial preliminary studies.

845 Theoretically, this slight benefit could be improved, as it is possible to obtain information from

846 the DNI maps with a spatial resolution corresponding to the size of individual SCAs, allowing a

847 more efficient local SCA focus controller. However, as **Kuhn et al. 2017a** pointed out, spatial

848 aggregation effects have a significant influence on the accuracy of ASI systems.

849 In this work we optimized the controller parameters according to the 7 combined spatial and

850 temporal DNI variability classes. In future works, it could be interesting to investigate the benefit

851 with individually optimized control parameters for each of the 40 theoretically possible

852 combinations of spatial and temporal DNI variability classes.

853 Furthermore, the used ASI system provides also predictions up to 15 minutes ahead. However,

854 currently we do not utilize the predictions for the power plant controller. A further improvement

855 could be achieved by including model predictive control strategies, which could utilize the

856 predictions.

857 The presented new control strategies are tailored to the La Africana solar field design. Other

858 power plants may have fundamentally different control approaches. Yet, to the best of our

859 knowledge the presented class dependent control strategies are the first which use classified

860 spatial DNI information. Spatial DNI information combined with the DNI classification procedure

861 represent additional input information, which could be beneficiary for any existing and future

862 parabolic trough solar field controller, regardless of the used overall control strategy.

863   Furthermore, we would like to point out that the potential benefit of spatial DNI information

864   combined with variability classification procedures is not limited to parabolic trough power plants.

865   Similar benefits might be feasible for other CSP technologies, such as Fresnel and point

866   focusing tower power plants. Benefits are also expected for solar PV power plants and electrical

867   grids.

868

Acknowledgment

References

878 Abutayeh, M., Alazzam, A., El-Khasawneh, B., 2014. Balancing heat transfer fluid flow in solar

879   fields, Sol. Energy, 105, 381-389. doi: 10.1016/j.solener.2014.03.025

880 Blanc, P., Massip, P., Kazantzidis, A., Tzoumanikas, P., Kuhn, P., Wilbert, S., Schüler, D., Prahl,

881   C., 2017. Short-Term Forecasting of High Resolution Local DNI Maps with Multiple Fish-Eye

882   Cameras in Stereoscopic Mode, AIP conference Proceedings 1850. doi: 10.1063/1.4984512

883 Burkholder, F., Kutscher, C., 2009. Heat Loss Testing of Schott's 2008 PTR70 Parabolic Trough

884   Receiver, Technical Report, NREL.

885 Chow, C.W., Urquhart, B., Lave, M., Dominguez, A., Kleissl, J., Shields, J., Washom, B., 2011.

886   Intra-hour forecasting with a total sky imager at the UC San Diego solar energy testbed. Sol.

887   Energy 85, 2881–2893. doi: 10.1016/j.solener.2011.08. 025.

888 Crăciun, BI., Kerekes, T., Séra, D., Teodorescu, R., Annakkage, UD.,2017. Power ramp

889   limitation capabilities of large PV power plants with active power reserves. IEEE Trans

890   Sustainable Energy, 8, 573-581. doi: 10.1109/tste.2016.2612121

891 Denholm, P., Margolis, R., 2016. Energy Storage Requirements for Achieving 50% Solar

892   Photovoltaic Energy Penetration in California, NREL/TP-6A20-66595, doi: 10.2172/1298934

893 Dersch, J., Hennecke, K., Quaschning, V.. 2012. Free Greenius – New Options and Availability.

894   In Proceedings of the SolarPACES 2012 Conference, Marrakesch (Marokko)

895 Dieckmann, S., 2017. DLR - Institut of Solar Research - greenius - The green energy system

896   analysis tool. URL http://www.dlr.de/sf/desktopdefault.aspx/tabid-11688/20442_read-44865/

897 García, I., Álvarez, J., Blanco, D., 2011. Performance model for parabolic trough solar thermal

898   power plants with thermal storage: comparison to operating plant data. Sol. Energy 95,

899   2443–2460. doi: 10.1016/j.solener.2011.07.002

900 Gevorgian, V., Booth, S., Review of PREPA technical requirements for interconnecting wind and

901   solar generation, NREL/TP; 5 D 00– 57089, 2013, available online:

902   http://www.nrel.gov/docs/fy14osti/57089.pdf

903 Giostri, A., 2012.Transient effects in linear concentrating solar thermal power plant, Ph.D. thesis,

904   Energy Department, Politecnico Di Milano http://hdl.handle.net/10589/89590

905 Hanrieder, N., Sengupta, M., Xie, Y., Wilber, S., Pitz-Paal, R., 2016. Modeling beam attenuation

906   in solar tower plants using common DNI measurements. Solar Energy 129, pp. 244-255. doi:

907   10.1016/j.solener.2016.01.051

908   Hirsch, T., Schenk, HE., 2010. Dynamics of oil-based parabolic trough plants—A detailed

909   transient simulation model. In Proceedings of the SolarPACES 2010 Conference, Perpignan

910   (France)

911   Hirsch, T., Martin, N., Gonzalez. L., Biencinto, M., Wilbert, S., Schroedter-Homscheidt, M.,

912   Chenlo, F., Feldhoff, J., 2014. Direct Normal Irradiance Nowcasting methods for optimized

913   operation of concentrating solar technologies, DNICast project, DNIcast Deliverable 2.1.

914   http://www.dnicast-project.net.

915   IRENA, 2019. Renewable capacity statistics 2019, International Renewable Energy Agency

916   (IRENA), Abu Dhabi. ISBN 978-92-9260-123-2

917   Janotte, N., 2012. Requirements for Representative Acceptance Tests for the Prediction of the

918   Annual Yield of Parabolic Trough Solar Fields, Ph.D. thesis, Fakultät für Maschinenwesen

919   der Rheinisch-Westfälischen Technischen Hochschule Aachen, Aachen Germany

920   Kazantzidis, A., Tzoumanikas, P., Blanc, P., Massip, P., Wilbert, S., Ramirez-Santigosa, L.,

921   2017. Short-term forecasting based on all-sky cameras, In: Renewable Energy Forecasting.

922   Woodhead Publishing Series in Energy. Woodhead Publishing, pp. 153–178. doi:

923   10.1016/B978-0-08-100504-0. 00005-6.

924   Kost, C., Shammugam, S., Jülch, V., Nguyen, H., Schlegl, T., 2018. Levelized cost of electricity

925   renewable energy technologies, Fraunhofer ISE,

926   https://www.ise.fraunhofer.de/en/publications/studies/cost-of-electricity.html

927   Kuhn, P., Nouri, B., Wilbert, S., Prahl, C., Kozonek, N., Schmidt, T., Yasser, Z., Ramirez, L.,

928   Zarzalejo, L., Meyer, A., Vuilleumier, L., Heinemann, D., Blanc, P., Pitz-Paal, R., 2017a.

929   Validation of an all-sky imager-based nowcasting system for industrial PV plants. Prog.

930   Photovolt.: Res. Appl. doi: 10.1002/pip.2968.

931   Kuhn, P., Wilbert, S., Prahl, C., Schüler, D., Haase, T., Hirsch, T., Wittmann, M., Ramirez, L.,

932   Zarzalejo, L., Meyer, A. and Vuilleumier, L., 2017b. Shadow camera system for the

933   generation of solar irradiance maps. Sol. Energy 157, 157–170. doi:

934   10.1016/j.solener.2017.05.074

935   Kuhn, P., Garsche, D., Wilbert, S., Nouri, B., Hanrieder, N., Prahl, C., Zarzalejo, L., Fernández,

936   J., Kazantzidis, A., Schmidt, T., Heinemann, D., Blanc, P., Pitz-Paal, R., 2019, Shadow-

937   camera based solar nowcasting system for shortest-term forecasts. Meteorologische

938   Zeitschrift (submitted)

939   Lilliestam, J., Barradi, T., Caldés, N., Gomez, M., Hanger, S., Kern, J., Komendantova, N.,

940   Mehos, M., Hong, WM., Wang, Z., Patt, A., 2018. Policies to keep and expand the option of

941   concentrating solar power for dispatchable renewable electricity. Energy policy, 116, 193-

942   197. doi: 10.1016/j.enpol.2018.02.014

943   Lilliestam, J., Pitz-Paal, R., 2018. Concentrating solar power for less than USD 0.07 per kWh:

944   finally the breakthrough?. Renewable Energy Focus, 26:17-21. doi:

945   10.1016/j.ref.2018.06.002

946   Marquez, R., Coimbra, C.F., 2013. Proposed metric for evaluation of solar forecasting models. J.

947   Sol. Energy Eng. 135 (1). doi: org/10.1115/1.4007496.

948   Mehos, M., Turchi, C., Jorgenson, J., Denholm, P., Ho, C., Armijo, K., 2016. On the Path to

949   SunShot: Advancing Concentrating Solar Power Technology, Performance, and

950   Dispatchability. Golden, CO: National Renewable Energy Laboratory. NREL/TP-5500-65688.

951   http://www.nrel.gov/docs/fy16osti/65688.pdf.

952   Noureldin, K., González-Escalada, L.M., Hirsch, T., Nouri, B., Pitz-Paal, R., 2016. Modelling and

953   optimization of transient processes in line focusing power plants with single-phase heat

954   transfer medium, AIP Conference Proceedings. Vol. 1734. doi: 10.1063/1.4949169

955   Noureldin, K., Hirsch, T., Pitz-Paal, R., 2017. Virtual Solar Field-Validation of a detailed transient

956   simulation tool for line focus STE fields with single phase heat transfer fluid. Sol. Energy146,

957   131–140. doi: 10.1016/j.solener.2017.02.028

958   Noureldin, K., Hirsch, T., Nouri, B., Yasser, Z., 2018a. Simulation of Potential Enhancements in

959   Parabolic Trough Solar Field Start-up Controllers using Nowcasting Systems. 24th

960   SolarPACES Conference (Casablanca, Morocco)

961   Noureldin, K., Hirsch, T., Kuhn, P., Nouri, B., Yasser, Z., Pitz-Paal, R., 2018b. Modelling an

962   automatic controller for parabolic trough solar fields under realistic weather conditions. AIP

963   Conference Proceedings. Vol. 2033. doi: 10.1063/1.5067211

964   Noureldina, K., Hirscha, T., Nouri, B., Yasserc, Z., Pitz-Paald, R., 2019a. Evaluating the

965   potential benefit of using nowcasting systems to improve the yield of parabolic trough power

966   plants with single-phase HTF. Applied energy (submitted)

967   Noureldin, K., 2019b. Modelling and Optimization of Transient Processes in Parabolic Trough

968   Power Plants with Single-Phase Heat Transfer Fluid. PhD Dissertation, RWTH Aachen,

969   Aachen (Germany)

970   Nouri, B., Röger, M., Janotte, N., Hilgert, C., 2018a Characterization and corrections for clamp-

971   on fluid temperature measurements in turbulent flows. Journal of Thermal Science and

972   Engineering Applications. Vol. 10, 031011.

973   Nouri, B., Kuhn, P., Wilbert, S., Prahl, C., Pitz-Paal, R., Blanc, P., Schmidt, T., Yasser, Z.,

974   Ramirez Santigosa, L., Heineman, D., 2018b. Nowcasting of DNI Maps for the Solar Field

975   Based on Voxel Carving and Individual 3D Cloud Objects from All Sky Images, AIP

976   Conference Proceedings. Vol. 2033. doi:10.1063/1.5067196

977   Nouri, B., Kuhn, P., Wilbert, S., Hanrieder, N., Prahl C., Zarzalejo, L., Kazantzidis, A., Blanc, P.,

978   Pitz-Paal, R., 2019a, Cloud height and tracking accuracy of three all sky imager systems for

979   individual clouds. Sol. Energy 177, 213–228. doi: 10.1016/j.solener.2018.10.079

980   Nouri, B., Wilbert, S., Segura, L., Kuhn, P., Hanrieder, N., Kazantzidis, A., Schmidt, T.,

981   Zarzalejo, L., Blanc, P., Pitz-Paal, R.,2019b, Determination of cloud transmittance for all sky

982   imager based solar nowcasting. Sol. Energy, 181, 251–263. doi:

983   10.1016/j.solener.2019.02.004.

984   Nouri, B., Wilbert, S., Kuhn, P., Hanrieder, N., Schroedter-Homscheidt, M., Kazantzidis, A.,

985   Zarzalejo, L., Blanc, P., Kumar, S., Goswami, N., Shankar, R., Affolter, R., Pitz-Paal, R.,

986   2019c. Real-Time Uncertainty Specification of all Sky Imager Derived Irradiance Nowcasts.

987   Remote Sens. 11(9), 1059. doi: 10.3390/rs11091059

988   Peng, Z., Yu, D., Huang, D., Heiser, J., Yoo, S., Kalb, P., 2015. 3D cloud detection and tracking

989   system for solar forecast using multiple sky imagers Sol. Energy 118, 496–519.

990   https://doi.org/10.1016/j.solener.2015.05.037.

991 Perez, R., David, M., Hoff, T.E., Jamaly, M., Kivalov, S., Kleissl, J., Lauret, P., Perez, M., 2016.

992   Spatial and temporal variability of solar energy. Found. Trends Renew. Energy 1 (1), 1–44.

993   doi: 10.1561/2700000006.

994 Pitz-Paal, R., 2017. Concentrating solar power: still small but learning fast. Nature Energy.

995   2(7):17095. doi: 10.1038/nenergy.2017.95

996 Platzer, WJ., 2016. Combined solar thermal and photovoltaic power plants–An approach to 24h

997   solar electricity?. AIP Conference Proceedings. Vol. 1734. doi: 10.1063/1.4949173

998 Quesada-Ruiz, S., Chu, Y., Tovar-Pescador, J., Pedro, H., Coimbra, C., 2014. Cloud tracking

999   methodology for intra-hour DNI forecasting. Sol. Energy 102, 267–275. doi:

1000   10.1016/j.solener.2014.01.030.

1001 Schlichting, T., 2018. Bewertung der Verwendbarkeit von Strahlungskarten für den Einsatz in

1002   der Regelung eines Parabolrinnensystems, Master thesis, Fakultät für

1003   Ingenieurwissenschaften, Universität Duisburg-Essen, Germany

1004 Schroedter-Homscheidt, M., Kosmale, M., Jung, S., Kleissl, J., 2018. Classifying ground-

1005   measured 1 minute temporal variability within hourly intervals for direct normal irradiances.

1006   Meteorol. Z. 2018. doi: 10.1127/metz/2018/0875.

1007 Wagner, PH., Wittmann, M., 2014. Influence of different operation strategies on transient solar

1008   thermal power plant simulation models with molten salt as heat transfer fluid. Energy

1009   Procedia, 49, 1652-1663. doi: 10.1016/j.egypro.2014.03.174

1010 Wilbert, S., Nouri, B., Prahl, C., Garcia, G., Ramirez, L., Zarzalejo, L., Valenzuela, L., Ferrera,

1011   F., Kozonek, N., Liria, J., 2016. Application of Whole Sky Imagers for Data Selection for

1012   Radiometer Calibration. In: EU PVSEC 2016 Proceedings, 1493–1498. doi:

1013   10.4229/EUPVSEC20162016-5AO.8.6

1014   Woyte, A., Van Thong, V., Belmans, R., Nijs, J., 2006. Voltage fluctuations on distribution level

1015   introduced by photovoltaic systems. IEEE Transactions on energy conversion, 21, 202-209.

1016   doi: 10.1109/TEC.2005.845454

1017   Zaversky, F., Medina, R., García-Barberena, J., Sánchez, M., Astrain, D., 2013. Object-oriented

1018   modeling for the transient performance simulation of parabolic trough collectors using molten

1019   salt as heat transfer fluid. Sol. Energy, 95, 192-215. doi: 10.1016/j.solener.2013.05.015